TECHNICAL MEMORANDUM

I-5490

A CROSSFLOW FORCE TRANSDUCER

by

T. M. Mulcahy

ARGONNE
NATIONAL
LABORATORY

BASE TECHNOLOGY

Prepared for
U. S. DEPARTMENT OF ENERGY
under Contract W-31-109-Eng-38

Printed in the United States of America
Available from
National Technical Information Service
U. S. Department of Commerce
5285 Port Royal Road
Springfield, VA 22161

NTIS price codes
Printed copy: A04
Microfiche copy: A01

TECHNICAL MEMORANDUM

ANL-CT-82-11
Distribution Category:
LMFBR--Components: Base
Technology (UC-79k)

ANL-CT--82-11

DE82 021141

ARGONNE NATIONAL LABORATORY
9700 South Cass Avenue
Argonne, Illinois 60439

A CROSSFLOW FORCE TRANSDUCER

by

T. M. Mulcahy

Components Technology Division

May 1982

TABLE OF CONTENTS

LIST OF FIGURES

MAJOR NOMENCLATURE

MAJOR NOMENCLATURE

b	Force-measurement ring width
C	Coherence
C_L	Lift-force coefficient
D	Cylinder diameter
E	Material elastic modulus
f	Frequency
f_v	Vortex shedding frequency
F_L	Lift force normal to cylinder axis and mean flow direction
F_D	Drag force in flow direction
GF	Gauge factor
H,K	Geometric parameters of force-measurement ring. See (3) and Fig. 2.
I	Turbulence intensity
ℓ	Length of force-measurement-ring beam sections
M	Magnitude of transfer function
M_n	n = 1, ..., 6. Moments at spring locations 1, 2, ..., 6 in Fig. 2.
N_R	Reynolds number
P	Phase of transfer function
q	Dynamic pressure
R	Radius of force-measurement ring
R_i	i = 1 to 8, strain-gauge resistances
SE	Internal strain energy
S	Input spectrum
t	Force-measurement-ring thickness (under strain gauge)
U	Mean flow velocity
V	Bridge excitation voltage
$\Delta V_D, \Delta V_L$	Bridge voltage change due to F_D, F_L
W	End plate spacing

α	Fraction of transducer ring radius R. See (2).
δ_L	Lift-direction deflection of transducer
$\Delta\varepsilon$	Minimum transducer bending strain
ε	Strain
ρ	Fluid mass density
σ_M	Maximum transducer bending stress
ϕ	Angle measurement. See Fig. 3.
ϕ_V	Lift-force spectral density (ℓ = 0.5 D)

A CROSSFLOW FORCE TRANSDUCER

by

T. M. Mulcahy

ABSTRACT

A force transducer for measuring lift and drag coefficients for a circular cylinder in turbulent water flow is presented. In adition to describing the actual design and construction of the strain-gauged force- ring based transducer, requirements for obtained valid fluid force test data are discussed, and pertinent flow test experience is related.

INTRODUCTION

Flow-induced vibrations of structures are a continuing concern in new power-generating system designs. As higher coolant flow rates are proposed to increase thermal capacity, the fluid forces on the structures are increased. A very efficient, and most typical, configuration for purposes of heat transfer is a circular tube in crossflow. To assess the fatigue or wear, the fluid forces acting on the structure are required to make a vibration analysis. Although the circular cylinder has been the most extensively studied bluff body in crossflow, knowledge of the fluid forcing function is lacking for many flow conditions, especially for the nonuniform, turbulent flows prevalent in reactor systems.

Theoretical prediction of flow-induced forces acting on bluff bodies is in the very early stages of development, and therefore experimental measurement of these forces must still be relied upon. Toward this end, a force transducer was sought to provide the fluid forces for vibration analysis of circular cylindrical beams in homogeneous, turbulent crossflow. A water medium was stipulated because the applications of interest are typically in dense fluids. Although the fluid forces on relatively rigid components could be obtainable with most fluid media and proper hydraulic scaling, the eventual goal is to measure the fluid forces where beam motion and fluid flow interaction occur. The required [1] simulation of relative structural and fluid mass are more convenient using dense fluids.

For analysis of beams, characterization of the force per unit length is required and can be accomplished in more than one way. The pressures at each point around the circumference of the cylinder can be measured and integrated to obtain the resultant force [2]. Alternatively, a force transducer whose sensing element is a finite-length circumferential segment (Fig. 1) of the cylinder has the advantage of measuring an integrated force per unit length directly [3]. The difficulty of the force-ring transducer is that rather complicated multicomponent sensing devices must be constructed in a small space for a wide variation in the character of the forces. However, a force-ring transducer was sought because of the difficulties in maintaining time references and amplitude scaling in the integration of pressure to obtain resultant forces, and because measurement of pressures in pressurized water also requires considerable instrumentation effort and interpretation of the data [4].

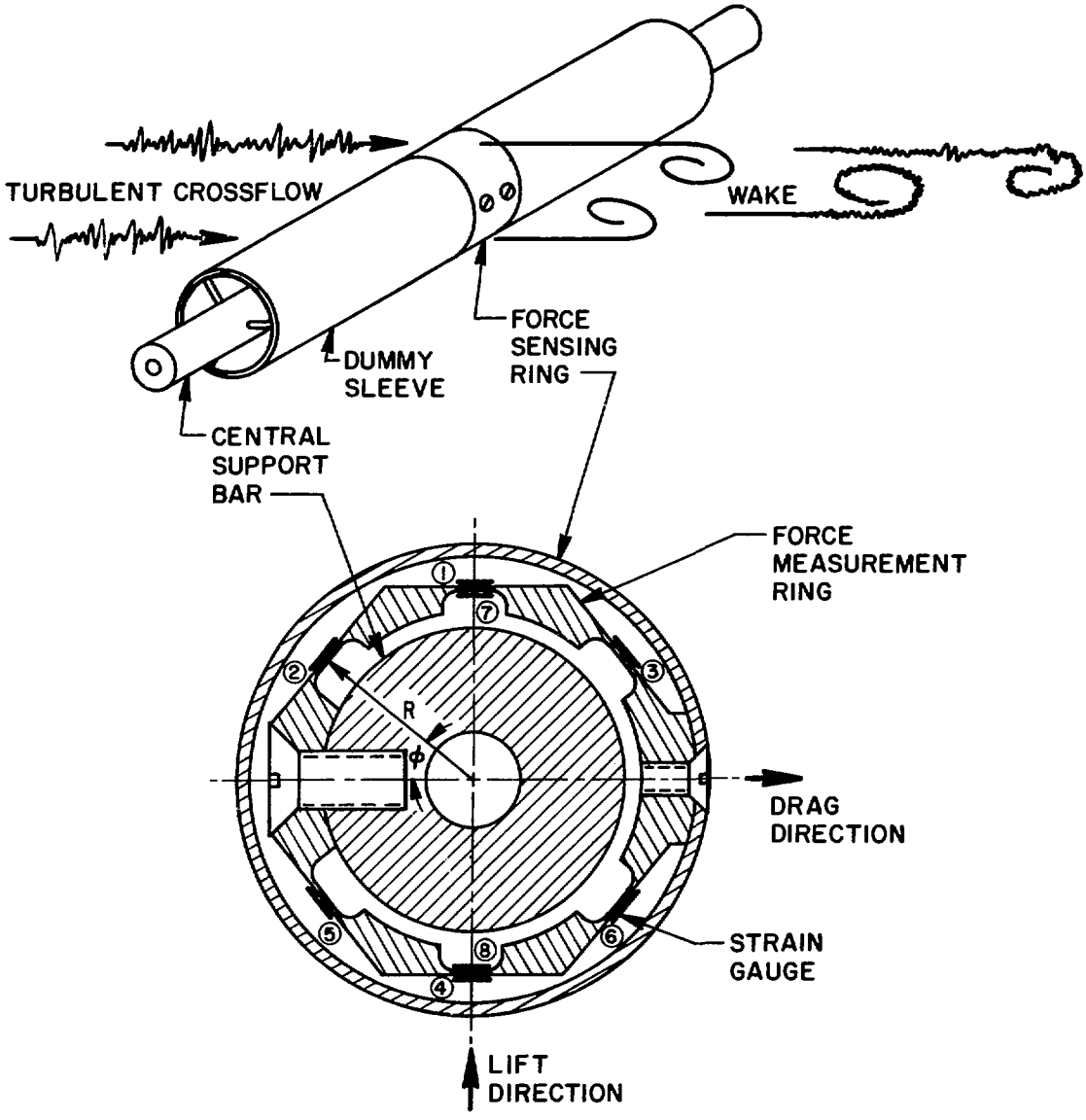

Fig. 1. Force transducer

The flow test facility available could provide a 0.31-m (12-in.)-square cross-section channel with flows up to 5.5 m/s (18 ft/sec) with an available pressure head of approximately one-half megapascal (~75 psi). A cylinder size of 25.4-mm (1-in.) diameter was chosen to minimize the need for blockage (8%) corrections to the fluid data. For this cylinder, the highest Reynolds number attainable is ~2 x 10^5. Grids were developed that produced turbulence intensities of 2-15% and length scales of 0.5-2 cylinder diameters. Forces on rigid cylinders in turbulent flow were not expected to be appreciably correlated beyond a length of three diameters, based on smooth flow results [5].

REQUIREMENTS

Three forces are of interest for a cylinder in crossflow: the steady drag force in the direction of the flow, the fluctuating drag force in the direction of flow, and the fluctuating lift force normal to the flow and the axis of the cylinder. The fluctuating forces are caused by a combination of vortices being shed in the wake and the turbulence in the flow. The interaction of the turbulence with the shed vortices is the subject of current research for which the force transducer is intended. A transducer was desired that could measure all the forces.

Information for establishing the transducer design criteria is limited because most force measurements have been made in smooth-flow wind and water tunnels where turbulence was maintained at a minimum. Turbulent flows have long been known to affect fluid forces, but only recently have efforts been made to quantify the effects for circular cylinders [2,7,8]. Although attenuated in intensity and broadened in spectral content by turbulence, vortex shedding remains a dominant source of the fluctuating forces in turbulent flows below transition Reynolds numbers of 3×10^5 based on mean flow velocity U and cylinder diameter D.

For low turbulence intensities, the lift-force frequency spectrum is contained in a narrow band centered around the frequency

$$f_v = 0.2U/D. \tag{1}$$

For intense turbulence the lift-force spectrum begins to look like the turbulent-velocity spectrum: a relative constant spectrum up to a cutoff frequency less than f_v. Because of the importance of the fluctuating lift force in production of beam vibrations, the lowest structural frequency of any force-measuring transducer should be well above f_v. A factor of 10 was considered adequate, based on a one-degree-of-freedom spring-mass system and limiting dynamic response at the vortex shedding frequency to 1% of the static deflection. The fluctuating drag force is usually an order of magnitude smaller than either the steady drag or the fluctuating lift force. It occurs at a frequency twice that of the fluctuating lift, where dynamic response of the transducer is an acceptable 4% of the static deflection.

Response at the resonant frequency which could mask the force signals was eliminated by low-pass filtering, a technique made possible by the

relatively high transducer resonant-frequency requirement. Without filtering the force signal, spurious signals due to transducer deformation at its resonant frequency could dominate the desired wake force signal. For instance, at a relatively high structural damping of 10% of critical damping, and assuming a force 10% as large as that occurring near the vortex shedding frequency, not an unreasonable estimate especially for small-scale highly turbulent flow, deformation of the transducer at resonance would be comparable to that caused by the vortex-shedding force, again based on a single-degree-of-freedom system.

Surface roughness is known to change the character of the vortex shedding process in ways similar to the expected effects of turbulence in the flow, and it therefore has to be minimized in order to study the effects of flow turbulence. Essentially, surface roughness influences the fluid forces in two ways: degradation of the correlation of the vortices along the length of the cylinder, and thickening of the boundary layer. The latter effect only occurs for very rough surfaces and will not be considered further. The former effect is of concern.

In nonturbulent flow across smooth, stationary cylinders, wake flow measurements [12] have shown that the vortices are shed as two-dimensional sheets, three to six diameters long, provided the mean flow Reynolds number based on the cylinder diameter is less than 10^5. As the flow Reynolds number is increased above 10^5, the attached boundary layer undergoes transition from a laminar to a turbulent flow regime. As a result, the two-dimensionality of the vortex shedding process is substantially degraded and the fluid forces are significantly decreased. Surface roughness can influence the vortex shedding process by causing premature transition of the boundary layer, with larger surface roughnesses creating earlier transitions and larger reductions in the associated fluid forces. However, disagreement exists in the literature on the threshold value for which the boundary layer is disturbed significantly: limits on the maximum roughness size from 10^{-3} to 10^{-6} of a diameter have been proposed or employed [3,9]. Machining of an acceptable surface finish, based on the most demanding limit, presented no difficulty. However, static deflection of the active force transducer ring with respect to the dummy sleeve (Fig. 1) was a concern. The relative deflection could not be made less than the upper limit while still maintaining a useful transducer sensitivity. Also,

construction of a dummy cylinder and a force sensing ring that are structurally separated by a circumferential gap less than 10^{-3} of a diameter was not possible. Maximum radial and longitudinal discontinuities of 10^{-3} of a diameter were adopted as being the best conditions for which the force-ring transducer could be constructed.

Perhaps more important than a surface roughness effect, pressure relief (venting) provided by the circumferential gap has been identified [13,14] as another mechanism that can greatly influence the axial correlation of the vortex shedding process, again by causing premature transition of the attached boundary layer. Even though the disturbance occurs at a single circumference along the cylinder axis, the effect is thought [15] to propagate over several diameters of cylinder length. The pressure relief can be solved by sealing the gap [7,14], but then transducer sensitivity and frequency response become a function of the sealant and usually the environmental conditions (especially temperature). Also, the sealed circumferential gap must be wider than an unsealed gap to provide a flexible connection relative to the transducer stiffness. As a result, the sealant introduces additional surface roughnesses which could be as effective as pressure relief in causing transition of the boundary layer. The circumferential discontinuities were rationalized as an unavoidable feature of the force-ring transducer, and the use of the transducer could only be justified by measurements which reproduce data in the literature. An unsealed circumferential gap was employed, but, as will be discussed later, end plates had to be employed to maintain the two-dimensionality of the vortex shedding process.

The range and magnitude of the fluid forces on the transducer ring were difficult to assess based on available data. Different turbulence intensities, length scales, blockages, and Reynolds numbers produce different force intensities and correlation lengths [7,8], and establishment of empirical relations to account for the effect of these parameters is the subject of current research. However, for a rigid cylinder, the maximum force in turbulent flow was not expected to exceed that in smooth flow. For the range of test Reynolds number, the steady drag-force coefficient is a nearly constant value of 1.1. The lift-force coefficient peaks in the Reynolds range of most interest, 10^4 to 1.5×10^5, with an average value of about 0.7. The coefficients are defined as the ratio of the force to the

product of the dynamic pressure and the projected area of the cylinder in the flow direction. These coefficients were employed in transducer strength considerations.

Flow turbulence affects these coefficients considerably; in particular, the lift coefficient becomes an exponentially decreasing function of Reynolds number in the range of interest [7,8]. Because the dynamic head increaases quadratically with Reynolds number in the same range, the lift is almost constant. A lift coefficient of 0.1 at a Reynolds number of 10^5 gave an estimate of the minimum force the transducer must resolve. Because the fluctuating drag can be very small in comparison to the other forces, its resolution for all flow condition was doubtful. Also, turbulence reduces the correlation of the forces along the length of the cylinder, with the longest correlation length of approximately three diameters expected in smooth flow. In turbulent flows, correlation lengths of a diameter or less were expected. To avoid underestimation of fluid forces due to lack of axial correlation, a force sensing ring one-half diameter long was employed. However, the design was based on a ring length of up to 3 diameters.

Contradictory information exists as to whether the amplitude of beam motion can influence the vortex shedding process and forces in turbulent flows. In nonturbulent flows very significant increases in the forces occur with increased amplitude of motion. A large part of the increase is due to increased correlation of the vortex shedding process along the length of the cylinder. However, evidence exists [7] that the fluid-structure interaction does not occur for turbulent flows having approximately 10% intensity. Yet practical examples of large-amplitude vibrations of chimneys, light poles, ocean piles, and reactor components, undoubtedly in turbulent flow, have been observed and thought to be due to vortex shedding and structural interaction. To avoid fluid/structural interaction effects, incorporation of the ring transducer on a rigid, stationary cylinder was planned, but a transducer design which can be incorporated on a flexible cylinder was desired for future studies.

A strain-gauged force ring [10] was chosen as the basic element of the transducer because of its relative stiffness for a given sensitivity, its ability to measure steady and dynamic components of force in two orthogonal directions, and its relative compactness for incorporation into a circular

cylindrical cross section without coupling to the deformation of the beam due to the flow or to the beam end supports.

A schematic of the force transducer mounted on the cylinder is shown in Fig. 1. The strain-gauged force-measurement ring is shown mounted on the central support bar in Fig. 2. Obviously the force-measurement ring that evolved is not a classic ring, but more a rigid frame with elastic beam joints where the strain gauges are mounted. Early analysis and testing showed a uniform-thickness ring did not yield both the desired sensitivity and rigidity. Sensitivity could be increased for the same stiffness by going to the rigid frame with beam joints concept. However, a desirable feature of a ring transducer was lost, since the strain gauges for monitoring the lift force F_L could not be located at a strain node of the drag force. A circumferential location of $\phi = 40°$ was chosen to equalize maximum strains and to facilitate construction.

For purposes of design, the transducer was idealized as a frame with rigid members connected by springs (see Fig. 3). The springs correspond to the thin flexible beams, of identical dimensions, which separate each rigid segment of the force-measurement ring shown in Fig. 1. The moments acting at each beam location

$$
\begin{aligned}
M_1 &= \frac{F_D R}{3} H + \frac{F_L R}{2} (1 + 2\alpha K), \\
M_2 &= -\frac{F_D R}{6} H + \frac{F_L R}{2} (1 + \cos\phi - \alpha K), \\
M_3 &= -\frac{F_D R}{6} H + \frac{F_L R}{2} (1 - \cos\phi - \alpha K), \\
M_4 &= -M_1 + 2\frac{F_D R}{3} H, \\
M_5 &= -M_2 - \frac{F_D R}{3} H,
\end{aligned}
\qquad (2)
$$

and

$$
M_6 = -M_3 - \frac{F_D R}{3} H,
$$

were determined by using the equations of equilibrium, symmetry, and compatibility of rotations around the perimeter of the frame. The moments are positive when the outside of the ring is in tension,

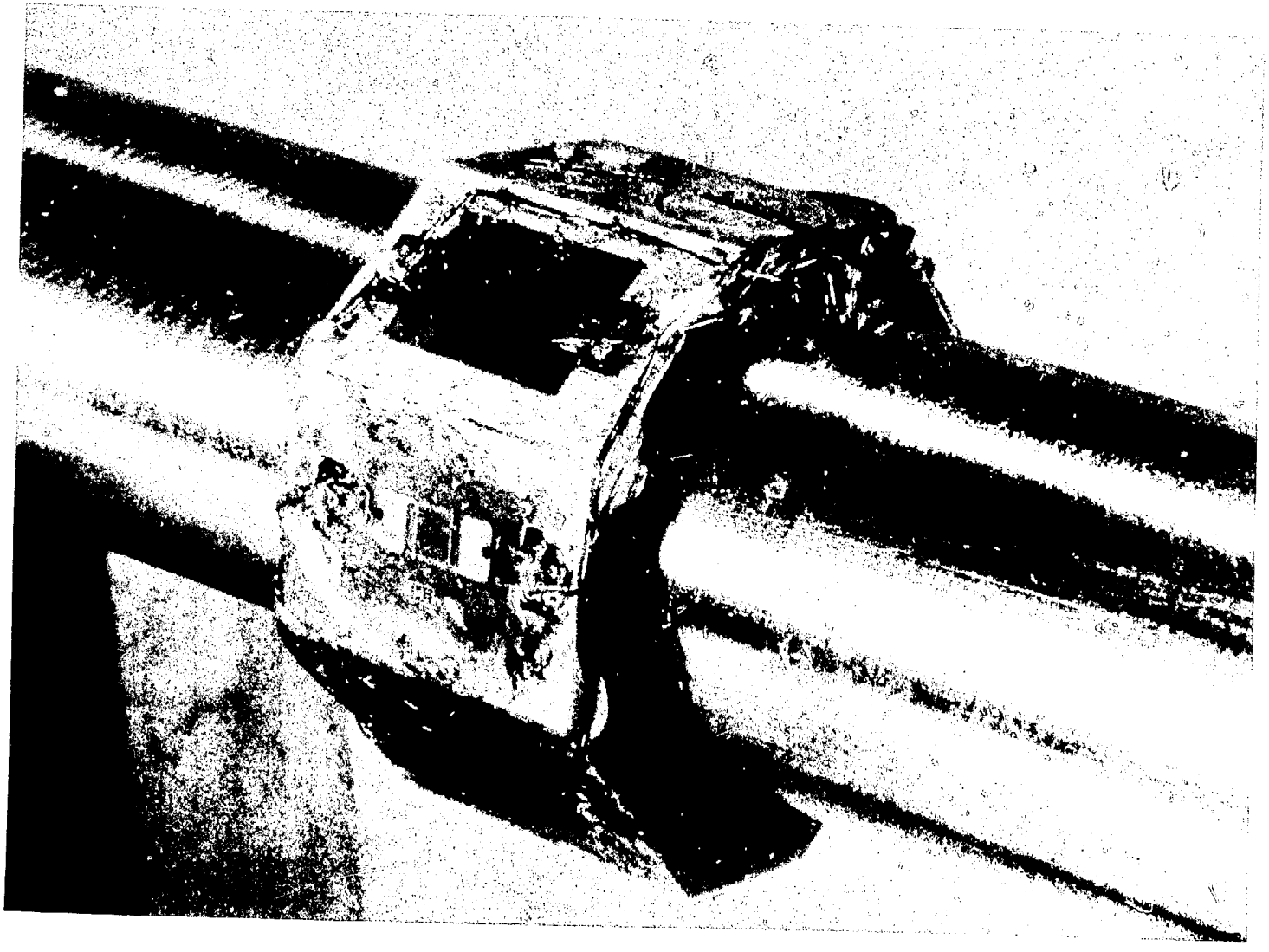

Fig. 2. Strain gauged, wired, and waterproofed force-sensing ring

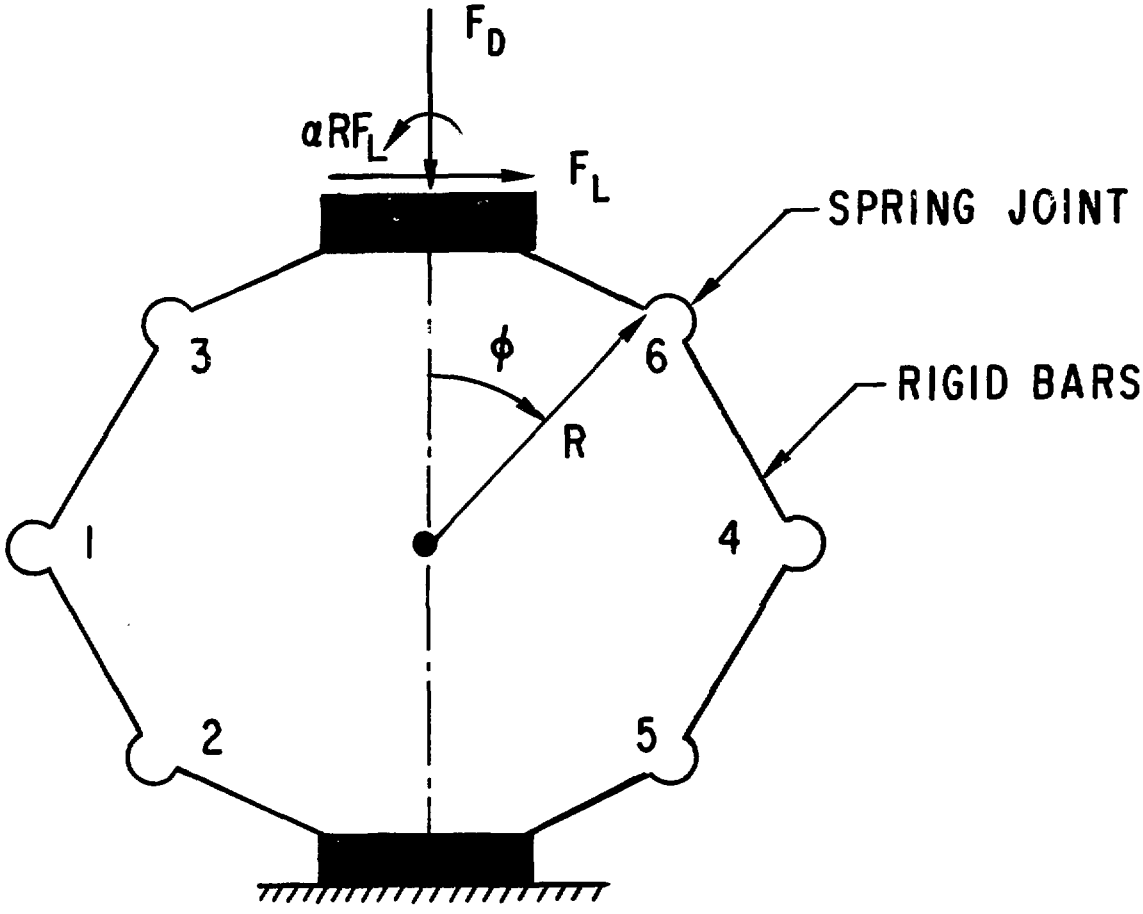

Fig. 3. Idealized rigid frame connected by springs (beams) at joints

$$H = 1 - \sin\phi,$$
$$K = H/(2 \sin\phi + 1), \tag{3}$$

and αR is the drag direction distance of F_L from the farthest upstream position of the transducer, the stagnation point.

Given the bending moments (2) and assuming strains due to axial loads are small in comparison to bending strains, the change in resistance for each strain gauge could be calculated. Employing nominally identical gauges in each leg, the sensitivities of the drag and lift force bridges were found to be

$$\frac{\Delta V_D}{V} = GF \frac{2RH}{Ebt^2} F_D, \tag{4}$$

and

$$\frac{\Delta V_L}{V} = GF \frac{3R \cos\phi}{Ebt^2} F_L. \tag{5}$$

The strain-gauge bridges are shown in Fig. 4, and the individual strain gauges are identified in Fig. 1. Note GF is the strain-gauge factor, E the transducer material elastic modulus, b the width of the transducer, and t the thickness of the transducer beam. Theoretically, the effects of the moment αF_L cancel out in both bridges, and the effects of F_D in the F_L bridge cancel and vice versa. In practice, minimization of cross sensitivity is a function of the accuracy of manufacturing identical beams with identical strain-gauge bridge legs.

Design strength loads were determined on the basis of a drag coefficient of 1.1 and a lift coefficient of 0.7. Thus, for an active transducer length of three diameters, a bound on the drag and lift forces in turbulent flow at the highest test Reynolds number was 32.0 N (7.2 lb) and 20.0 N (4.5 lb), respectively. Inspection of the moments (2) shows that the largest moment occurs for locations 2 and 5, with a value of 0.183 N-m (1.62 lb-in.), when the lift force is assumed to act through the center of the cylinder, $\alpha = 1$. To achieve a sensing-ring length of one-half tube diameter, the width of the measurement-ring was chosen as 12.7 mm (0.5 in.). A measurement-ring radius of R = 10.2 mm (0.4 in.) was chosen based on ease of fabrication. Thus, the maximum bending stress σ_M expected occurred at locations 2 and 5 and was

$$\sigma_M = \frac{86.46}{t^2}, \tag{6}$$

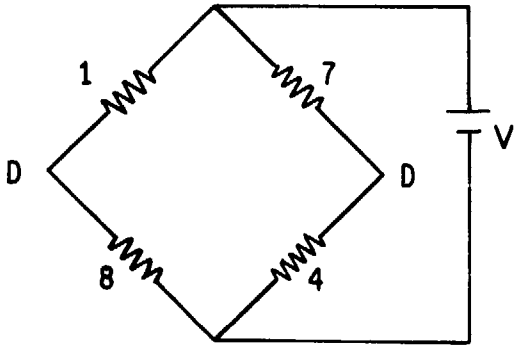

$$\frac{\Delta V_D}{V} = \frac{R_7 R_8 - R_1 R_4}{(R_1 + R_8)(R_7 + R_4)}$$

(a)

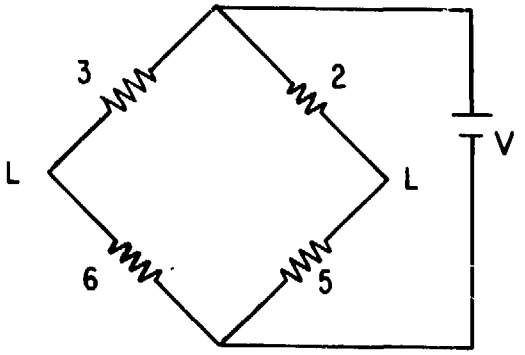

$$\frac{\Delta V_L}{V} = \frac{R_6 R_2 - R_3 R_5}{(R_3 + R_6)(R_2 + R_5)}$$

(b)

Fig. 4. Strain-gauge bridge for: (a) F_D and (b) F_L

in MPa for t measured in millimeters.

Static deflection of the transducer δ_L in the direction of an applied force F_L was determined utilizing the moments (2) and Catigliano's theorem: $\delta_L = \partial SE/\partial F_L$, where SE is the total internal strain energy. The maximum deflection was expected in the lift direction and for F_L = 20.0 N (4.5 lb) was

$$\delta_L = \sum_{n=1}^{6} \frac{12 \ell M_n}{Ebt^3} \frac{\partial M_n}{\partial F_L} = 1.85 \times 10^{-2} \frac{\ell}{t^3} , \tag{7}$$

in millimeters when ℓ, the length of the beam section of the measurement ring, and t are in millimeters. In deriving (7), only the bending deformation of the transducer ring beams was assumed to contribute to the total strain energy. Theoretically ℓ can be reduced to achieve any desired stiffness but practically it is limited by the strain-gauge size.

The minimum (lift) force of interest, 0.22 N (0.05 lb), occurred at a Reynolds number of 10^5, for a lift coefficient of 0.1, on the shortest active force ring length of 12.7 mm (0.5 in.). Since the strains at gauges 2 and 5 of Fig. 1, due to the lift force, are about a factor of seven larger than the others in the lift-force bridge, the minimum strain $\Delta\varepsilon$ to be resolved could be determined utilizing the moment at gauge 2 due to F_L:

$$\Delta\varepsilon = \frac{3R(1 + \cos\phi)}{Ebt^2} F_L = \frac{4.54 \times 10^{-6}}{t^2} , \tag{8}$$

with t in millimeters. The elastic modulus of a steel alloy 2.06×10^{11} Pa (30×10^6 psi) was assumed.

Several iterations of the thickness to determine a design showed that the primary constraints on the design were imposed by the minimal strain requirement (8) and the maximum allowable deflection (7). The thickness chosen, t = 0.38 mm (0.015 in.), maintained the minimum strains of interest above 25 $\mu\varepsilon$. This was considered the minimum strain allowable to avoid effects of nonlinear time-dependent behavior of the transducer material [11]. An ℓ = 2.0 mm (0.08 in.) was chosen to allow easy installation of relatively large strain gauges to minimize backing and bond-line creep. The corresponding stiffness of the transducer according to (7) was found to be

$$\frac{\delta}{F_L} = 3.43 \times 10^{-2} \frac{\text{mm}}{\text{N}} \left(6 \times 10^{-3} \frac{\text{in.}}{\text{lb}}\right) . \tag{9}$$

Thus, to minimize the static transducer deflection to less than 0.03 mm (0.001 in.), the fluid loading in the lift direction would have to be maintained below 0.74 N (0.167 lb). This is considerably less than the 20-N (45-lb) load anticipated on the longest (3 diameters) active transducer ring.

Because the maximum fluid-force estimates were thought to be considerably larger than those which would actually occur, a transducer was constructed, instrumented, calibrated, and tested. Even if the force estimates were accurate, the transducer would be usable for a force-sensing ring of one-half diameter. The transducer material chosen was 17-4 Ph stainless steel whose yield stress 7.585×10^8 Pa (110,000 psi) was more than twice that expected according to (6), again desirable to avoid nonlinear transducer material behavior [11]. The expected sensitivities of the transducer according to (4) and (5) were determined to be

$$\frac{\Delta V_D}{V F_D} = 3.91 \times 10^{-5} \text{ N}^{-1} \left(1.74 \times 10^{-4} \text{ lb}^{-1}\right) \tag{10}$$

and

$$\frac{\Delta V_L}{V F_L} = 1.26 \times 10^{-4} \text{ N}^{-1} \left(5.61 \times 10^{-4} \text{ lb}^{-1}\right), \tag{11}$$

assuming a gauge factor of 2.

CONSTRUCTION

The force-measurement-ring material was chosen to be 17-4 PH stainless steel, not only because of its desirable load-deflection characteristics, but also because of its resistance to the corrosive effects of the deionized water used in the test facility where the force measurements were made. In machining the measurement ring, particular attention was given to obtaining: uniform thickness (±3% of nominal) and polish (64 finish) of all six webs where the strain gauges were mounted (see Fig. 1), parallelism (0.005-mm deviation per mm length) between the generators of the two cylindrical surface segments where the measurement ring is mounted to the central support bar and where the sensing ring is mounted to the measurement ring, and orthogonality and/or parallelism (0.005 mm/mm) of the web surfaces with respect to the other webs in the same bridge circuit. These machining practices were followed to maintain deformation symmetry between various webs of the measurement ring, and, thus, maintain the validity of the bridge equations (10-11) and minimize cross sensitivity. Also, normality of the deflection of the transducer with respect to the axis central support bar was maintained such that the small circumferential gap between the force-sensing ring and the dummy sleeve did not close completely upon maximum transducer deformation.

Before the measurement ring was strain-gauged, it was mounted on the central support bar along with the brass dummy sleeve and the stainless steel force-sensing ring. The three-point adjustment, provided for each dummy sleeve at two axial locations, allowed close concentric positioning with respect to the central support bar while still allowing rotation with respect to the support bar and the force-sensing ring. With such an alignment, the tube ends of the force-sensing ring and the dummy sleeve could be lapped together (expedited by use of a lathe) to form a very narrow and uniform circumferential gap on each end of the force-sensing ring. Subsequently, the dummy sleeves could be locked onto the central support bar, and the entire unit, shown in Fig. 1, turned on a lathe to obtain smooth transitions between the cylindrical surfaces of the sensing ring and the dummy sleeve.

The transducer elements were marked for position and then disassembled, except for the sensing ring, which was strain-gauged in place. Polyimide-encapsulated, constantan alloy foil gauges 1.59 mm (0.062 in.) in

length, with a thermal-expansion coefficient similar to that of the transducer material, were the largest readily available (M≡M's WA-06-062ED-120) strain gauges which could be fit on the webs of the transducer. A 350-Ω resistance would have been more desirable from the standpoint of gauge excitation optimization, but only 120-Ω resistance was available. The gauges were glued under pressure with epoxy (M≡M AE-15) and cured @ 75°C for one hour. The bridge circuits were completed on the force-sensing ring (see Fig. 2), with magnet wire (34 AWG) having a polyurethane coating. Further insulation was provided by three coats of GE Gylptal cured at 50°C in a vacuum for ~16 hr. In retrospect, a first coating with an insulating acrylic (M≡M M-CoatD) and then Gylptal coatings provided a better barrier against electrolysis of the copper wire. After several weeks of usage, a crack in the varnish surfaces allowed an intergauge lead wire to be etched completely through. The white acrylic appears to provide a more flexible layer, not subject to cracking, which allows better visual inspection of the coverage compared to the transparent Gylptal. Note that the Gylptal dissolves M-CoatD.

Upon completion of strain gauging and waterproofing, the transducer was reassembled and the original alignment was recovered. After the disassembly and repair of the open intergauge wire, the original alignment could only be recovered by gluing the force-sensing ring on the force-measurement ring using the dummy sleeves as jigs. Acrylic dental cement could be easily drilled out for future disassembly. The transducer assembly shown in Fig. 1 was mounted in the test section utilizing end supports which penetrated the test-section wall (see Fig. 5). End clamps secured the transducer assembly from the axial and rotational motion which was desirable for alignment of the transducer's drag-direction with respect to the flow direction. The end supports and clamps also provided a pressure seal. To prevent cavitation of the turbulence generator grids, static pressures up to 5.52 Pa (80 psi) were employed. In Fig. 6, the transducer assembly with end support plates and clamps is shown loosely assembly and outside the test section.

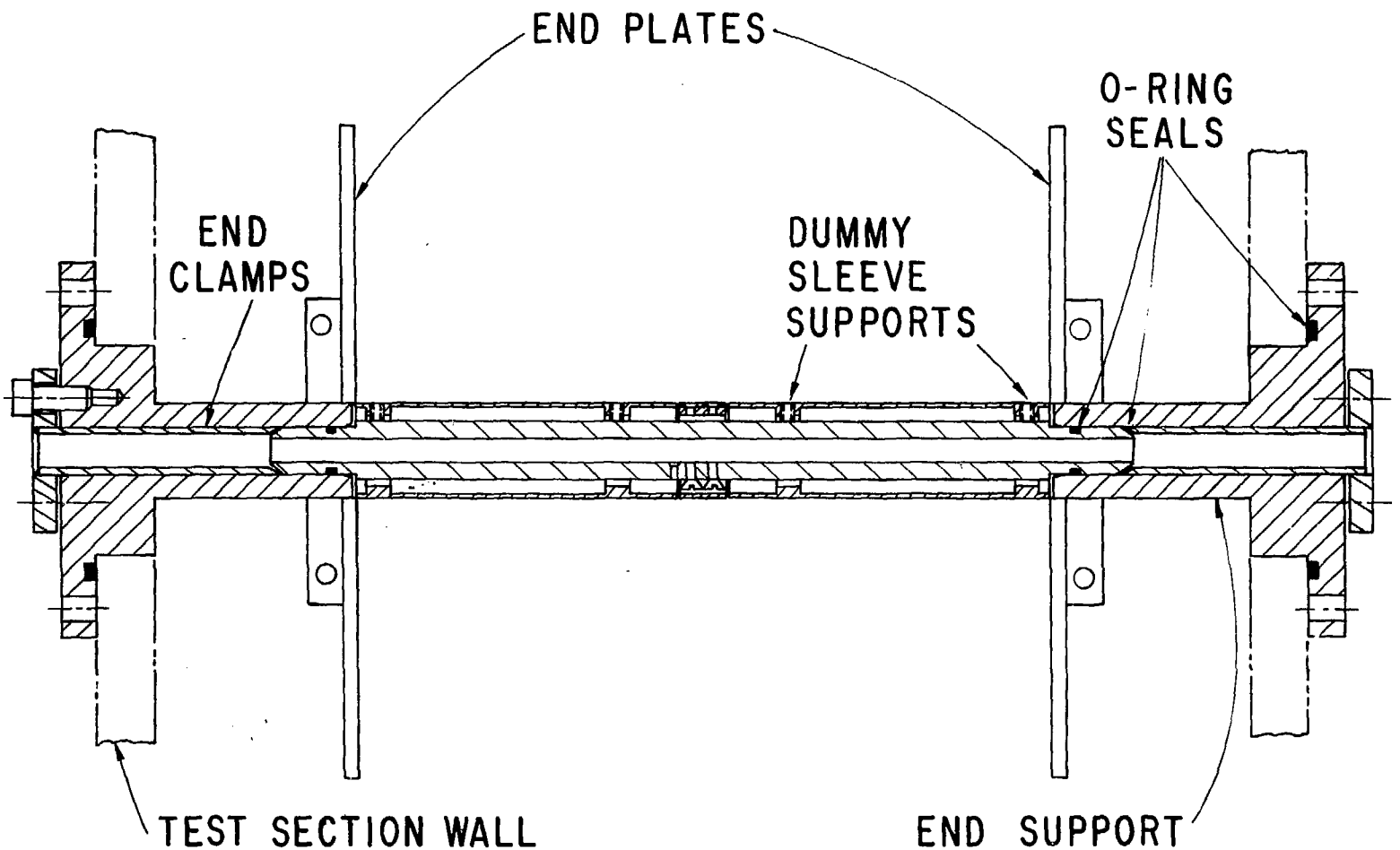

Fig. 5. Force-transducer assembly mounted in end supports attached to test-section walls

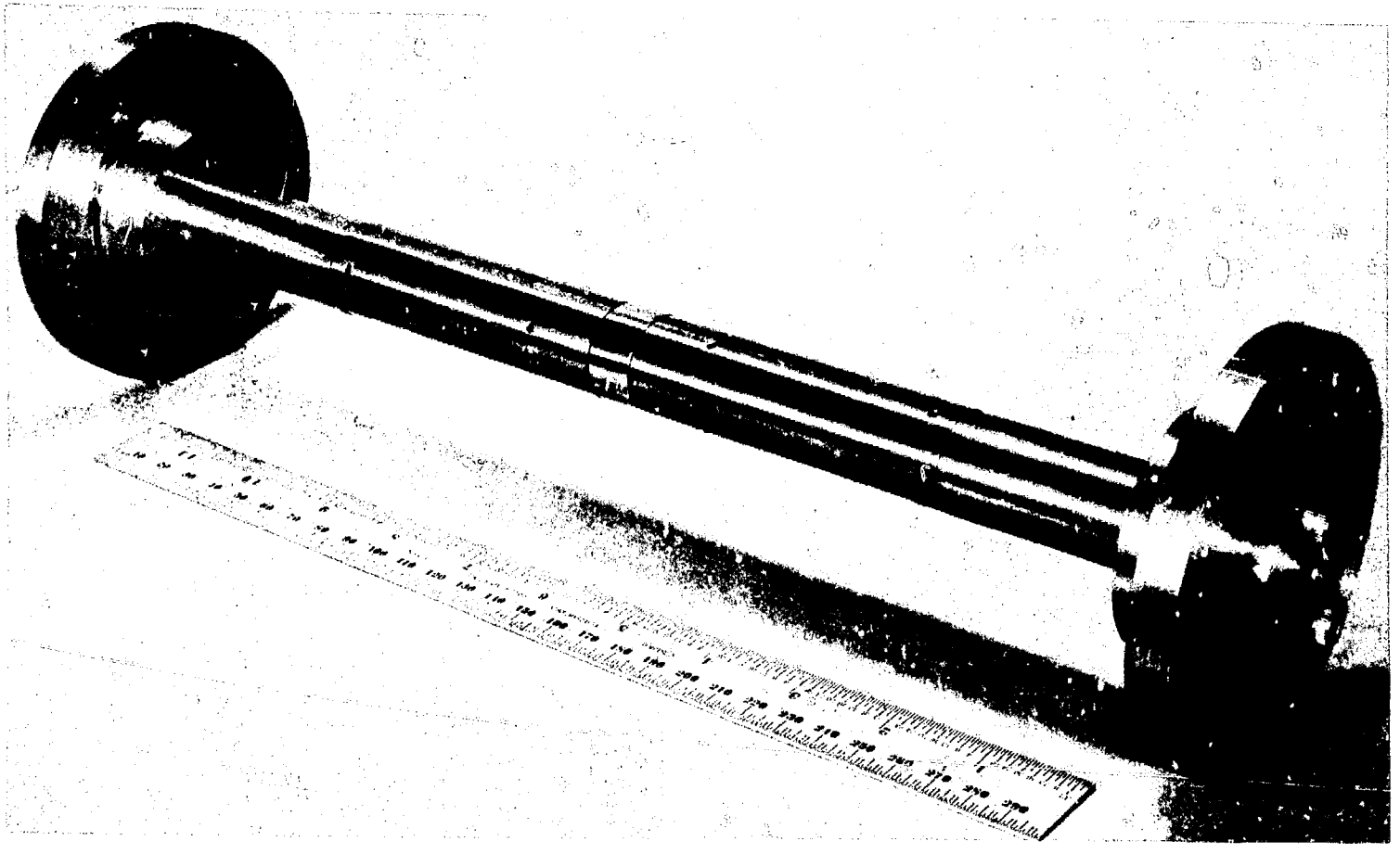

Fig. 6. Force-transducer assembly loosely assembled in end supports

INSTRUMENTATION AND CALIBRATION

An Unholtz-Dickie Model D22PMB Bridge Conditioning Amplifier was employed to provide 6-V bridge excitation, bridge balance (automatic mode), and low-pass filtering (100 or 1000 Hz) of the signal. Bridge excitation greater than 6-V caused zero-balance drift. Most of the data signals occurred below 100 Hz. However, most of the data was taken utilizing the 1000-Hz low-pass filter because the 100-Hz filter has a linear but severe phase shift with increasing frequency.

Both static and dynamic calibrations of the force transducer were performed. The static sensitivity of the transducer was measured by hanging known weights from the force-sensing ring. Measurements were made over the weight range 0.05-5.0 N (0.011-1.1 lb) which was the expected fluid-force range. The bridge amplifier sensitivity and gain were adjusted to give a nominal system sensitivity of 2.148 V/N (0.483 V/lb). The measurement error ±5% was caused by thermal oscillations and transducer creep. Seven data points were taken, beginning at 0.05 N (0.011 lb), with an approximate doubling of the weights between measurement points. The data were graphed, and a straight line could be drawn within the ±5% error bounds for each data point. The corresponding bridge sensitivities were $\Delta V_L/(VF_L) = 1.27 \times 10^{-4}N^{-1}$ ($5.65 \times 10^{-4}lb^{-1}$) and $\Delta V_D/(VF_D) = 3.37 \times 10^{-5}N^{-1}$ ($1.50 \times 10^{-4}lb^{-1}$), which are close to the predicted values (10-11), especially in the lift direction.

The static calibrations discussed above were performed by placing the weight through the geometric center of the force-sensing ring. Because the fluid force is not necessarily applied through the center, the transducer was designed to be insensitive to the force-application location. To assess this design feature, similar calibrations were performed with the weights applied at the extreme off-center locations, tangential to the force-sensing ring. The results were the same. However, cross sensitivity between the F_L and F_D measurement directions was greatest for off-center loading, but never exceeded 4%. By rotating the transducer and measuring output peaks due to an applied weight, the F_L and F_D axes were found to be 92° (±1°) apart. However, the axes were rotated from line of transducer symmetry by ~7°, which was accounted for by transducer marking. These angular orientations can be measured and identified much more accurately than the mean flow direction orientation in turbulent flow.

Dynamic calibration of the force transducer was performed mainly to assess the desired constancy of the system transfer function over the frequency range of interest (<100 Hz); static calibration was considered a more accurate method of absolute calibration because better control of the very small applied forces was possible. The value of the transducer's lowest natural frequency and the character of the associated resonant response were investigated by dynamic testing. By treating the force-measurement ring as a single-degree-of-freedom massless spring supporting the mass of the 12.7-mm (0.5-in.)-long force-sensing ring, a ~350-Hz fundamental frequency in air was predicted using the stiffness given in (9). By plucking the sensing ring and inspecting the decay curve and spectrum of the output signal, a 395-Hz resonant structural frequency with ~1% critical damping was measured. Assuming that submergence of the transducer in water causes the effective mass of the sensing ring to be increased by an added mass [5] equal to twice the displaced mass of water, a fundamental frequency of ~207 Hz was predicted. During testing in turbulent flow, a natural frequency of 267 Hz with 1.6% of critical damping was measured from spectral densities of the transducer output.

Although the in-air lowest natural frequency of the transducer was nearly 10 times larger than the highest expected fluid-forcing frequency (~50 Hz), the submerged frequency was only 5 times larger. To ensure spurious signals from transducer resonance were not present, impact tests with an instrumented force hammer were made to determine the transfer function. An impact pad for a commercially available impulse hammer (PCB Model K2981A02) was developed to produce small-magnitude, low-frequency loads typical of those expected during flow testing. After encapsulating the lead wire and connector for the hammer's piezoelectric (voltage mode) force transducer (PCB 208A02), the transfer functions for 10 tests were calculated and averaged utilizing a fast Fourier-transform spectral analyzer (HP 5451B). (See Appendix A.)

The average input-force spectrum (S), transfer function, magnitude (M) and phase (P), and coherence function (C) are shown in Figs. 7 and 8. The desirable constancy of the transfer function is apparent, but the sensitivities determined in the dynamic tests were typically 10-15% lower than the static calibration sensitivities. These differences were attributed to difficulties encountered in dynamic testing: striking the force-sensing

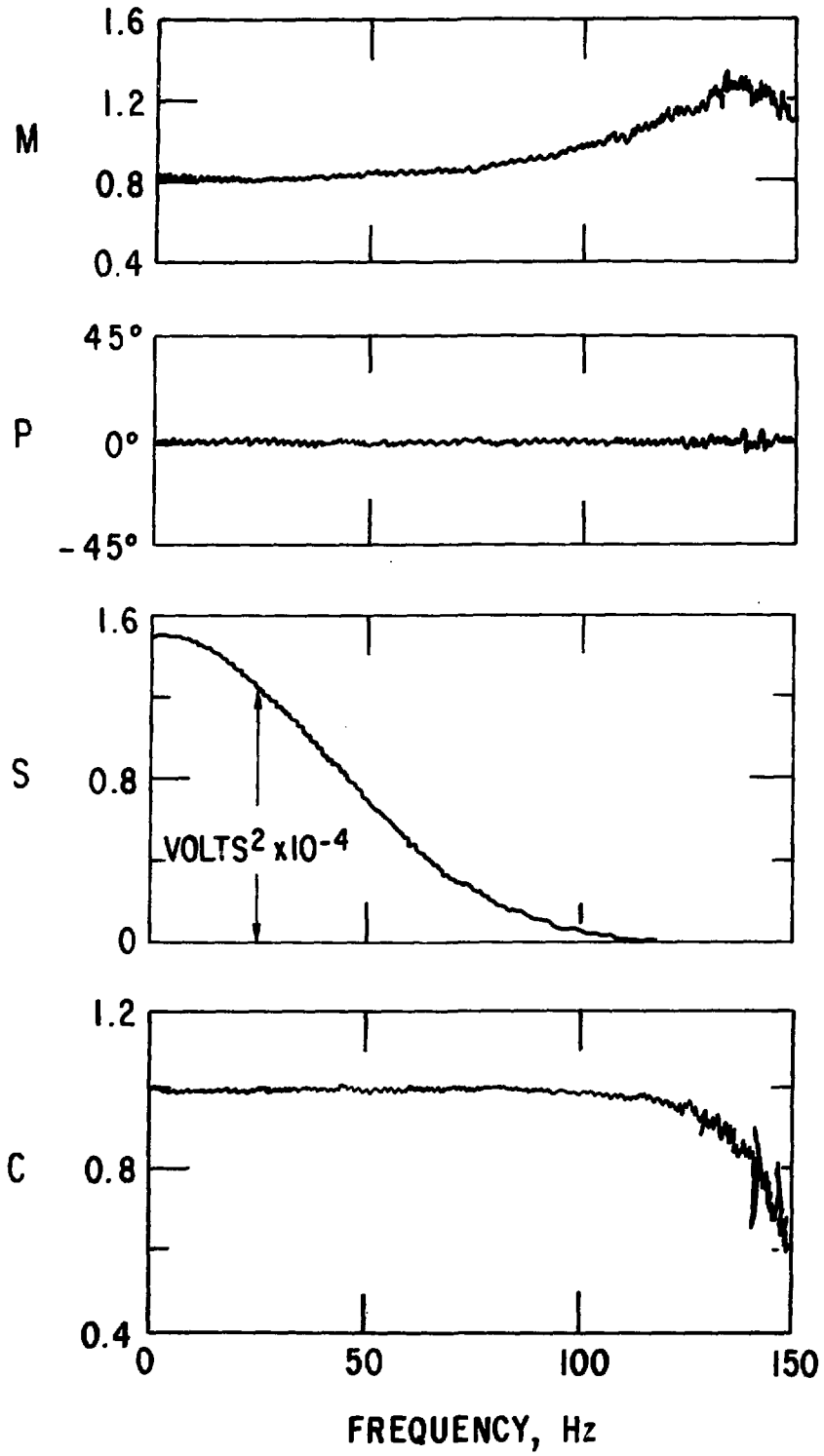

Fig. 7. The transfer function magnitude M and phase P, input spectrum S, and coherence C for lift-direction excitation of the transducer in water

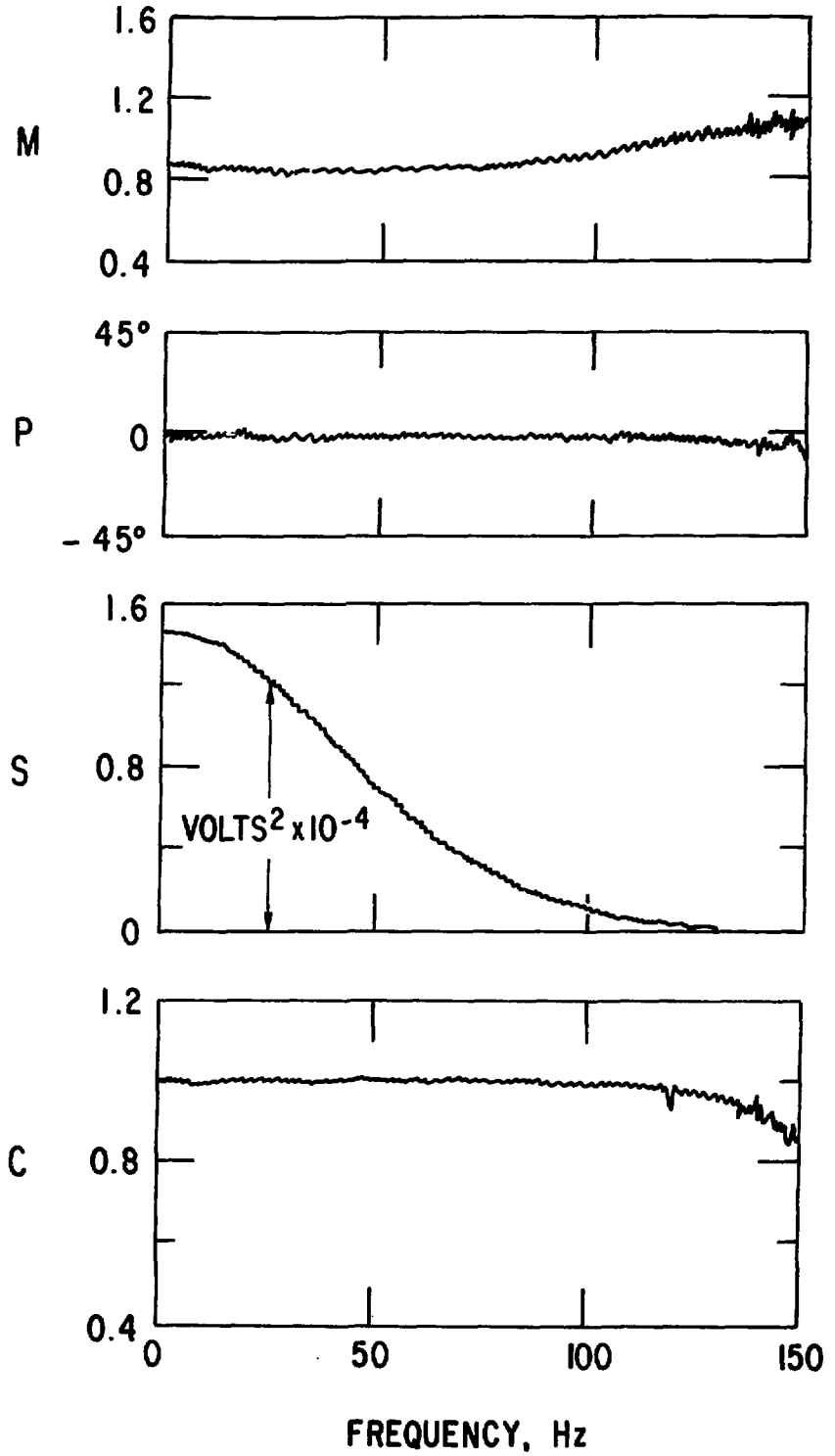

Fig. 8. The transfer function magnitude M and phase P, input spectrum S, and coherence C for drag-direction excitation of the transducer in water

ring in exactly the lift or drag direction, and impulse-hammer inertia effects, which cause the hammer's force-transducer signal to indicate a larger force magnitude than was actually applied. (See Appendix A.) The static calibration sensitivities were employed in data analysis.

TEST EXPERIENCE

Before addressing experiences associated with actual flow testing, a more mundane problem will be discussed. Although self-compensated temperature gauges were used, not enough space physically existed on the transducer to make each bridge circuit self-temperature compensating [21]. As a result, upon startup of the flow for testing, cooler water would circulate into the confined transducer-location space and cause a significant bridge imbalance. This problem was circumvented by zeroing the bridges at 10% or less of the test flow rate. Since the forces are proportional to flow velocity squared, no corrections to the data were required.

The test program in which the crossflow force transducer was used studied the effects of different flow turbulence intensities I and integral scale lengths L on the fluctuating lift-force coefficient. The I measures the size of the velocity fluctuations in the flow direction as a percentage of the mean flow U, while L is an average measure of the corresponding turbulent eddy size. Designers use C_L to determine the lift force/length F_L according to

$$F_L = C_L\left(\frac{1}{2}\,\rho U^2 D\right). \tag{12}$$

The lift-coefficient data normally are presented as a function of Reynolds number N_R and any other varied parameters: cylinder yaw, cylinder motion, surface roughness, flow turbulence, etc. To date most of the data have been obtained for a smooth surface cylinder in nonturbulent flow ($I < 0.5\%$) which is both rigid and stationary, and it is included in Fig. 9. The effects of cylinder yaw and motion have received considerable attention, but research on the other parameters is just beginning.

Fluctuating lift-force coefficients were determined with the crossflow force transducer utilizing the same equipment employed in calibration. Several water flows with different turbulence characteristics were tested over the Reynolds number, N_R, range 10^4 to 2×10^5. The transducer signals were conditioned, captured by the spectrum analyzer, digitized, and average spectral densities were calculated. The spectrums were integrated, and the results were normalized by the mean flow dynamic pressure $[(1/2)\rho U^2]$ and the projected flow area (ℓD) to give the root-mean-square value of the lift-force coefficient C_L.

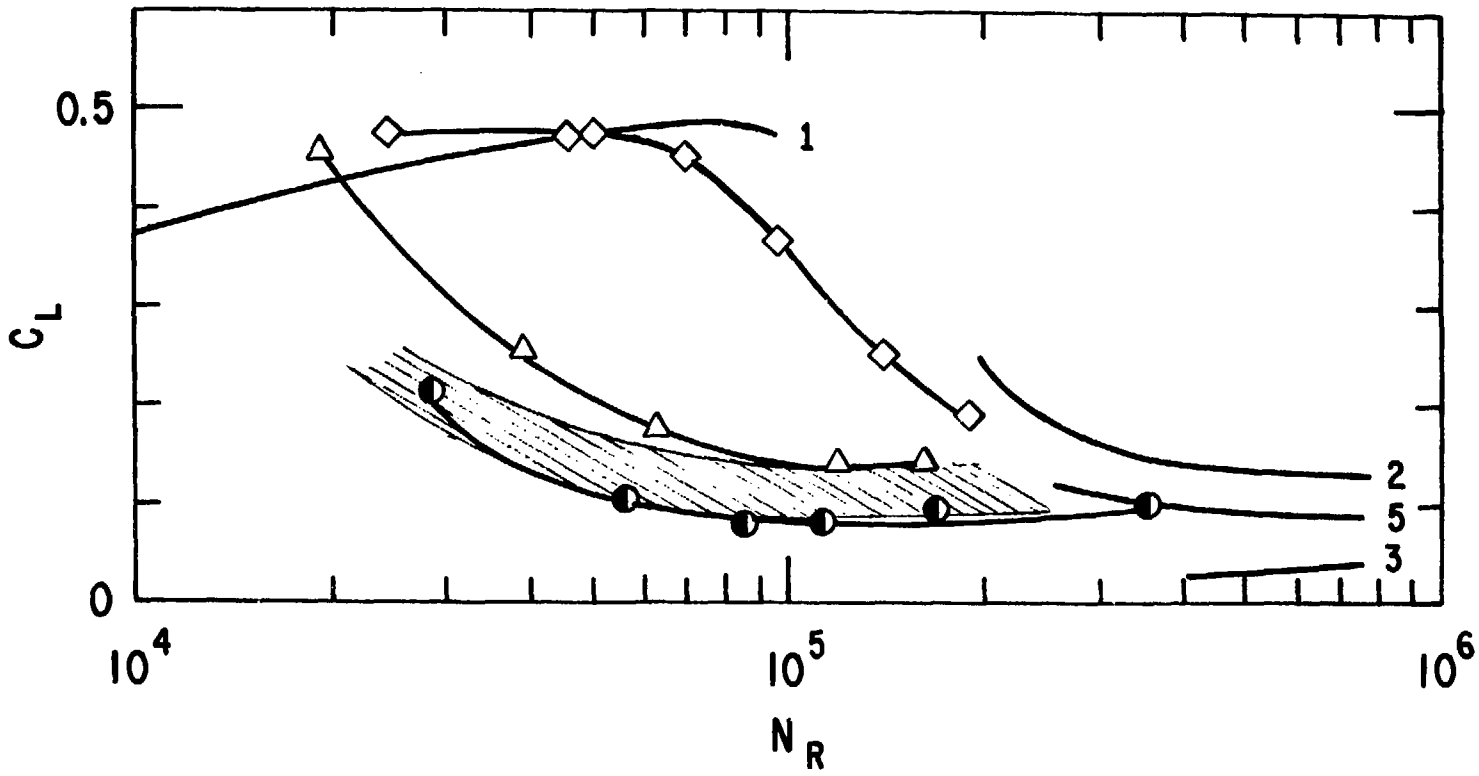

Fig. 9. Lift-force coefficients for nonturbulent flow: 1 [14], 2 [17], 3 [18], and 5 [16]. For turbulent flow: without end plates ▨ ; with end plates ◇ (I = 3%, L/D = 2.0), Δ (I = 15%, L/D = 1.0), and ◐ (I = 16%, L/D = 0.4)

Initial testing was performed to verify that the construction of the crosflow transducer, essentially the circumferential gaps between the force-sensing ring and the dummy sleeves, was not interfering with the vortex shedding process: causing premature transition from a laminar to a turbulent, attached boundary layer. The nonturbulent flow data for C_L available in the literature and shown in Fig. 9 show that a significant reduction in C_L can be expected at $N_R \cong 2 \times 10^5$ due to the transition. Although turbulence intensities in the test section employed could not be made smaller than ~2%, transition Reynolds numbers and force coefficients close to those obtained in nonturbulent flow were expected.

However, the initial tests gave very low, nearly the same, values of C_L for all the turbulent flows ($2 < I < 15\%$). This indicated transition of the turbulent boundary layer had occurred over a wide range of Reynolds numbers ($2 \times 10^4 < N_R < 2 \times 10^5$) where laminar, attached boundary layers were expected. (See the crosshatched data band in Fig. 9.) Another indicator of a turbulent, attached boundary layer is a nearly random force signal, at least, compared to the relatively periodic force signal which occurs for a laminar boundary layer. However, inspection of the shape of the calculated spectral densities showed periodic (narrow frequency band) signals for low-turbulence flows at some N_R. (See Fig. 10.) Transition of the boundary layer could have been partial, leading to these contradictory indicators. But instead of further investigating the boundary-layer condition, design modifications to the force transducer and flow test-section were made to circumvent the anomaly.

Several attempts were made to fill the circumferential gap with sealant, but none were successful. In most cases the sealant simply provided too strong a reinforcement, such that all transducer sensitivity was lost. When the bound was flexible enough, the transfer function was poor. The circumferential gap could have been sufficiently widened to produce a flexible seal with a good force-transducer transfer function, but the inevitable roughness of the sealant surface raised as many questions as problems solved. Covering the force-sensing ring and dummy sleeves with a continuous thin rubber sheet (a stretched balloon, smooth side up) provided a slightly less sensitive transducer with an adequate transfer function. However, the transfer function for the surface-covered transducer was sensitive to temperature and the deterioration of the adhesive (Permatex

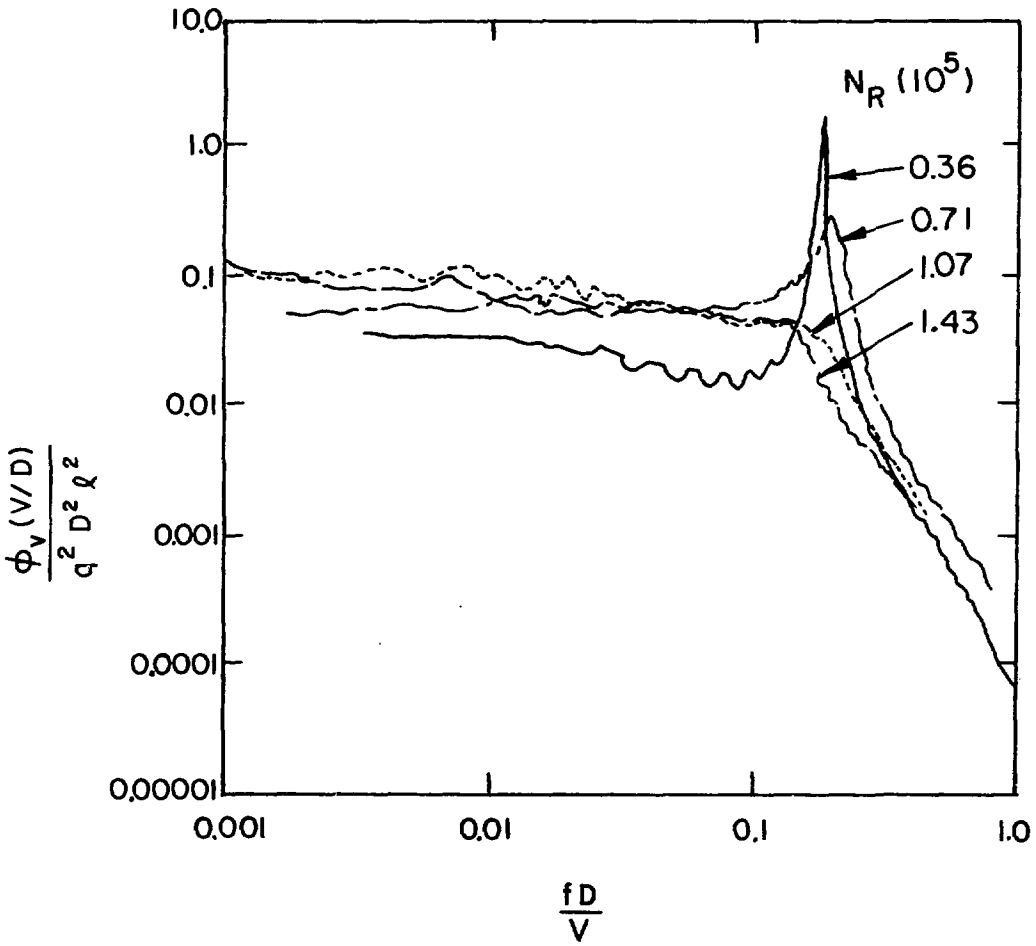

Fig. 10. Normalized lift-force spectrums for I = 4% and L/D = 0.5

adhesive-sealant No. 99GA) line in the vicinity of the circumferential gap. Data were obtained with transducer calibration performed, at temperature and in water, before and after flow testing. The results were similar to those obtained without the surface covering.

Having eliminated the circumferential gap as the source of the low lift-coefficients, the use of end plates to maintain two-dimensionality of the wake vortex shedding was investigated. Leakage flow through small annular gaps between the test cylinder and the wind-tunnel walls, as well as the flow channel wall's boundary-layer flow, have been shown [12-18,19] to propagate along the cylinder, interact with the wake flow, and significantly affect the force coefficients and the base pressure in the stagnant region immediately downstream of the cylinder. To prevent such interactions, which make test results unique to the particular flow channel employed, many investigators have employed two end-plates. They are mounted on and normal to the cylinder axis and placed symmetrically on each side of the force-sensing ring. (See Fig. 5.) The spacing, size, and shape of the end-plates are somewhat controversial, but a recent study [19] has identified a design that avoids creating a boundary layer on the end-plates which interacts with the wake flow. Square end-plates, 178 x 178 mm (7 x 7 in.), which were 3.18 mm (0.125 in.) thick, were constructed for evaluation testing. The center of the hole for the cylinder was placed equally far from the top and bottom of the plate but at 2.5D from the rounded leading edges of the end-plates.

Since the selection of the remaining end-plate variable, their lateral separation, appears to depend upon the particular flow channel employed, a series of flow tests was performed at different spacings W. The lift coefficients obtained for flows with the same, relatively small, turbulence intensity are shown in Fig. 11. Apparently the end-plates at W/D = 6.5 and 7.5 increase the lift coefficients to values comparable to those obtained in nonturbulent flow, but smaller spacings of W/D = 5.0 and 3.5 increase the lift coefficients even more. Similar measurements have been made [14] in a much larger wind tunnel, where aspect ratios up to 30D were possible. The results were similar for small spacings: the lift coefficients increased with decreasing W for W/D $\leq$ 5 and were the same for 5 $\leq$ W/D $\leq$ 7.5. For larger W the results were different: in the wind-tunnel study the lift coefficients remained constant until W/D = 15 and then decreased

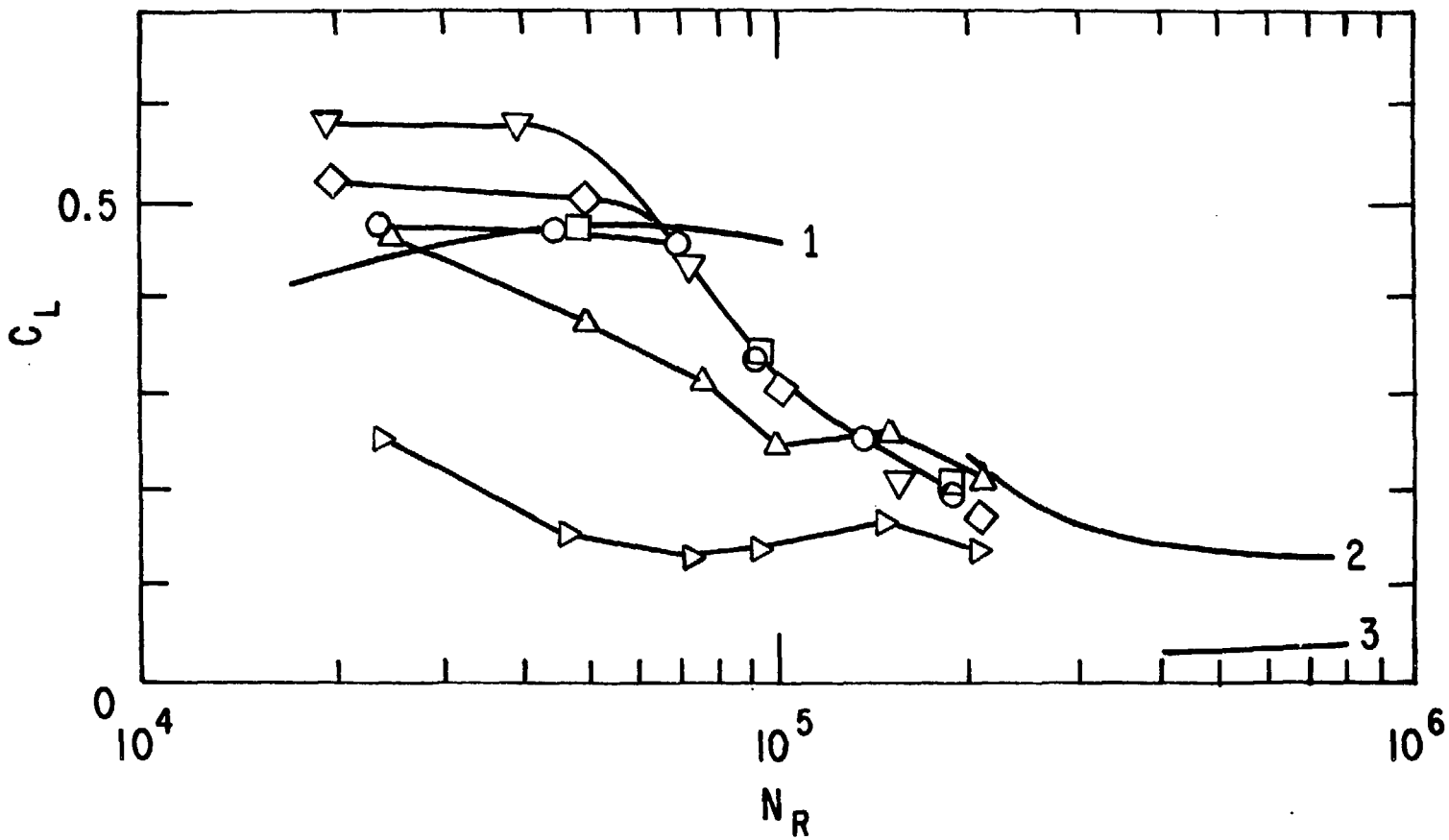

Fig. 11. Variation in C_L, for I = 3% and L/D = 2, with end-plate spacing W. (Symbol, W/D): ▷, 12; △, 9.75; ○, 6.5; □, 7.5; ◇, 5.0; ▽, 3.5. Nonturbulent flow curves: 1 [14], 2 [17], 3 [18]

significantly, whereas the data in Fig. 11 show a rapid decrease, with increasing W, for W/D > 9.75. The differences were attributed to the differences in channel size, and a spacing of 6.5-7.5D was employed in the test.

The fact that vortex shedding in nonturbulent flow has been found [12] to be significantly correlated over an axial distance (cell) of approximately six diameters is considered significant. End-plates are believed [20] to isolate, from destruction by end effects, the highly correlated cells of vortex shedding which naturally occur in two-dimensional flow. Therefore W/D < 6 were never considered for use in the test, because the vortex shedding process apparently is strengthened from that which occurs in two-dimensional flows. Of course this same line of reasoning raises another question about the use of these data by a designer. Do end effects and flow variations in practical flow naturally produce three-dimensional vortex shedding and turbulent attached boundary layers? This is a difficult question which can only be investigated, much less answered, on a case-by-case basis. However, the force coefficients obtained with the transducer and end-plates described above are thought to yield, at least, upper bounds on the forces which occur in practical turbulent flows. But these upper bounds are not nearly as large, in many cases, as those previously obtained in nonturbulent, two-dimensional flow. Thus the results obtained with the transducer should be valuable in optimizing designs.

ACKNOWLEDGMENTS

The work reported was supported by the U.S. Department of Energy, Office of Reactor Research and Technology, under Contract W-31-109-Eng-38.

REFERENCES

1. "Flow-Induced Vibration Testing Sc .e Modeling Relations," Presented at ASME Pressure Vessel Piping Tec .nology Conference, San Francisco, Aug 12-15, 1980. Flow Induced Vi ation Design Guidelines, ed. P. Y. Chen, ASME PVP 52, 111-126 (1981).

2. Surry, D., "Some Effects of Inte .e Turbulence on the Aerodynamics of a Circular Cylinder at Subcritic . Reynolds Number," J. Fluid Mech. 8(3), 543-563 (1972).

3. Richter, A., and Naudascher, E., "Fluctuating Forces on a Rigid Circular Cylinder in a Confined Flow," J. Fluid Mech. 28(3), 561-576 (1976).

4. Mulcahy, T. M., Wambsganss, M. W., and Lawrence, W., "Dynamic Surface Pressure Instrumentation for Rods in Parallel Flow," Presented at 1980 SESA Spring Meeting, Boston, Mass, and in Exp. Mech. 22 (1), 31-36 (1982).

5. Blevins, R. D., Flow-Induced Vibration, Von Nostrand Reinhold, 1977.

6. Goldstein, S., Modern Developments in Fluid Dynamics, Vol. II, 1965.

7. Savkar, S. D., and So, R. M. C., "On the Buffeting Response of a Cylinder in a Turbulent Crossflow," Technical Information Services Report No. 78CRD119, Research and Development Center, General Electric Co. (1978).

8. So, R. M. C., and Savkar, S. D., "Buffeting Forces on Rigid Circular Cylinders in Crossflows," J. Fluid Mech. 105, 297-425 (1981).

9. Szechenyi, E., "Supercritical Reynolds Number Simulation for Two-dimensional Flow over Circular Cylinders," J. Fluid Mech. 70(3), 529-542 (1975).

10. Cook, N. H., and Rabinowicz, E., Physical Measurement and Analysis, Addison-Wesley, 1963.

11. Tovey, F. M., "Transducer Flexure Material Behavior," Measurements and Control 11(6), 94-100 (1977).

12. Farell, Cesar, "Flow Around Fixed Circular Cylinders: Fluctuating Loads," J. Eng. Mech. Div., ASCE 107(EM3), 565-588 (1981).

13. Schmidt, L. V., "Measurements of Fluctuating Air Loads on a Circular Cylinder," J. Aircraft 2(1), 49-55 (1965).

14. Keefe, R. T., "An Investigation of the Fluctuating Forces Acting on a Stationary Circular Cylinder in a Subsonic Stream and of the Associated Sound Field," University of Toronto Institute for Aerospace Studies Report 76 (1961).

15. Bearman, P. W., "On Vortex Shedding from a Circular Cylinder in the Critical Reynolds Number Regime," J. Fluid Mech. 37(3), 577-585 (1969).

16. Loiseau, H., and Szechenyi, E., "Analyse Expérimentale Des Portances sur un Cylindre Immobile soumis a un Ecoulement Perpendiculaire a son Axe a des Nombres de Reynolds Elevevés," La Recherche Aerospatial, No. 5, 279-291 (1972).

17. Fung, Y. C., "Fluctuating Lift and Drag Acting on a Cylinder in a Flow at Supercritical Reynolds Numbers," J. Aerospace Sci. 27(11), 801-814 (1960).

18. Schmidt, L. V., "Fluctuating Force Measurements upon a Circular Cylinder at Reynolds Numbers up to 5×10^6," Meeting on Ground Wind Load Problems in Relation to Launch Vehicles, NASA Langley Research Center, June 7-8, 1966, NASA TM 47779, pp. 19.1-19.17 (1966).

19. Stansby, P. K., "The Effects of End Plates on the Base Pressure Coefficient of a Circular Cylinder," Aeronaut. J. 78, 36-37 (1974).

20. Mair, W. A., and Stansby, P. K., "Vortex Wakes of Bluff Cylinders in Shear Flow," SIAM 28(2), 519-539 (1975).

21. Dorsey, J., "Homegrown Strain-gage Transducers," Exp. Mech. 17(7), 255-260 (1977).

APPENDIX A - FORCE TRANSDUCER TRANSFER FUNCTION

To determine the transfer function for the crossflow force transducer, a commercially available impulse hammer (PCB Model K2981A02) was employed to produce a known transient input. The input from the submerged hammer and the output from the submerged crossflow force transducer were conditioned and analyzed with a two channel fast-Fourier-transform spectrum analyzer (HP 5451B). (See Fig. A-1.) The results for 10 tests were averaged to obtain a transfer function. Details are provided below.

As produced, the physical size and weight of the impulse hammer were heavier than desirable for producing force transients having the low magnitudes and frequency content typical of the fluid force loading. Since a smaller, more sensitive impulse hammer was not readily available, a special felt impact tip (see Fig. A-2) was developed for the piezoelectric force transducer (PCB 208A02) incorporated in the hammer, and an additional factor-of-10 amplification was provided (CEC 1-163) to the factor-of-10 amplification already provided by the power/amplifier unit (PCB 480A06). (See Fig. A-2.) The signal from the force transducer was filtered (GR 1952) out above 250 Hz (low-pass) before connecting to the input of the two-channel FFT-spectrum analyzer (HP 5451B). The signal from the force-measurement-ring strain gauge bridge, balanced and amplified with a bridge amplifier (UD-D22), was filtered in the same way before connection to the output channel of the spectrum analyzer.

Before the transfer function of the crossflow force transducer was determined, the impulse hammer was calibrated in two steps. First, a piezoelectric force transducer, identical to the one incorporated in the impulse hammer, was calibrated by quickly lifting known weights off the transducer face. Upon liftoff of the weight, the piezoelectric transducer's peak discharge voltage was proportional to the weight. The results from eight tests, utilizing several weights in the range of interest, were averaged with a resultant sensitivity of 12.35 mv/N (2.278 mv/lb). The maximum deviation of the tests was ~1.5%, and the manufacturer's sensitivity for the piezoelectric transducer was given as 11.82 mv/N (2.656 mv/lb).

The second step involved use of the impulse hammer to impact the calibrated piezoelectric transducer, immobilized in a relatively heavier vise (see Fig. A-2), and determination of the hammer transfer function utilizing a setup similar to Fig. A-1 with the calibrated piezoelectric force

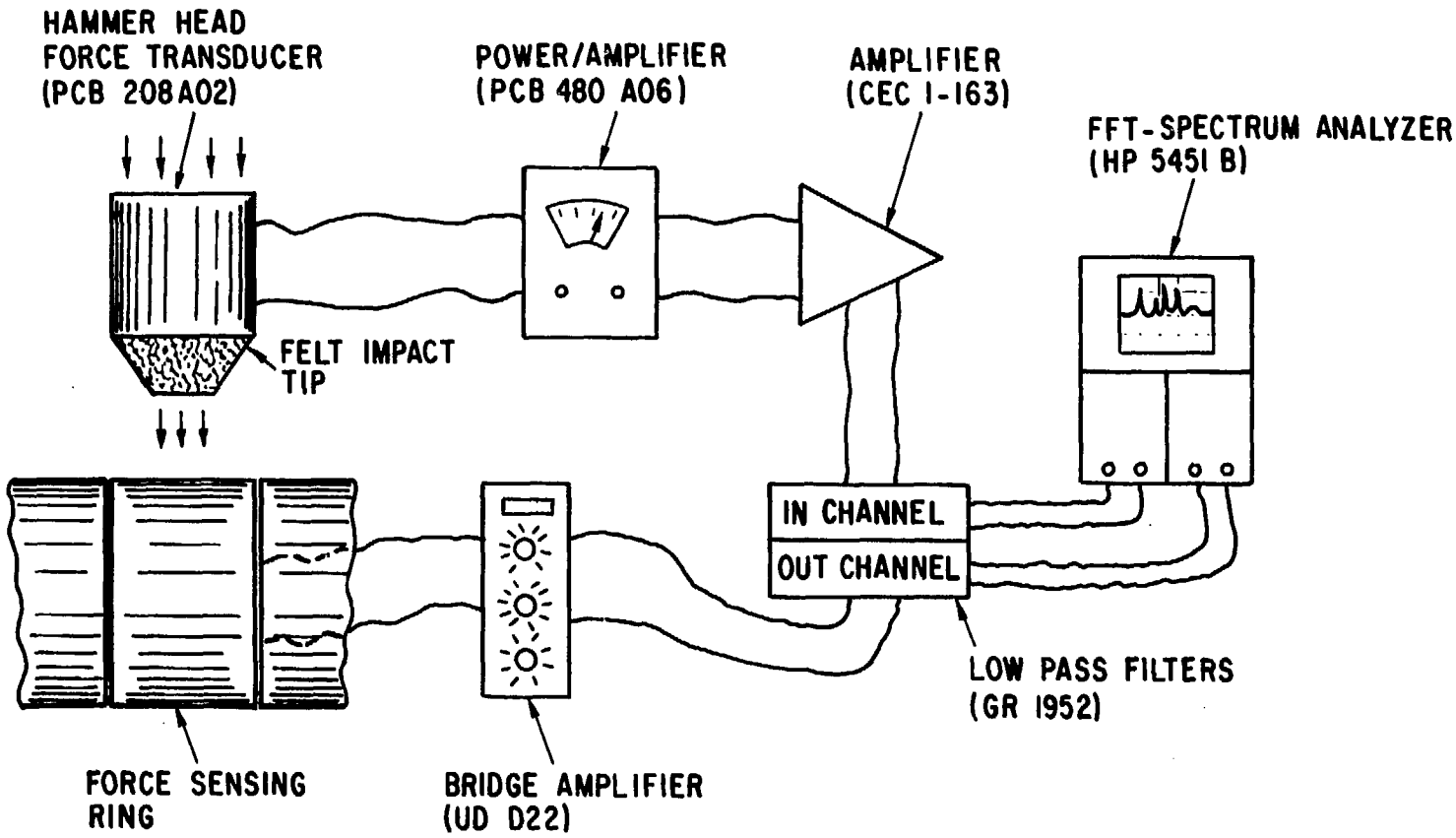

Fig. A-1. Calibration setup schematic

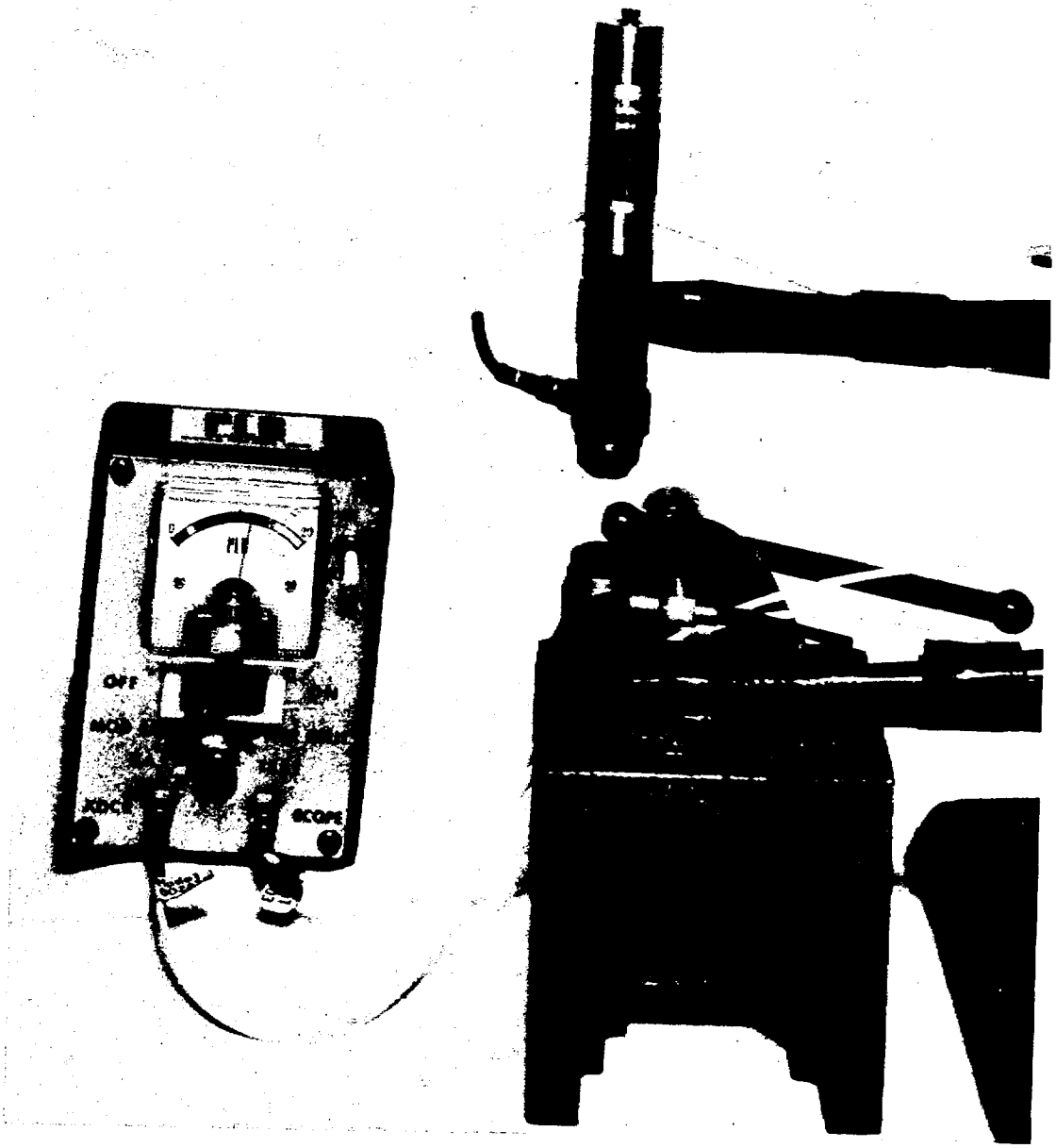

Fig. A-2. Impulse hammer with modified impact cap

transducer replacing the crossflow force transducer. The results from 10 trials were averaged, and the transfer function's magnitude and phase were found to be nearly constant over the frequency range of interest. Also complete coherence was determined for the same frequency range. The transfer-function magnitude was found to be 1.20, with a maximum deviation of 2.3% from 0 to 150 Hz. Over the same frequency range, the phase of the transfer function was essentially zero with a maximum deviation of 0.85°. Note the impulse hammer is 20% less sensitive than the isolated piezoelectric force transducer.

Besides being essential, calibration of the impulse hammer served several purposes. Many impact tests were performed prior to hammer calibration to shape the impact tip of the impulse hammer so that a force transient with the desired frequency content was produced. Also, a feeling for correct impacting, without double striking, was developed. Most importantly, a modification of the recorded time transient of the impulse hammer was found necessary. Because of the weight of the hammer and the increased sensitivity of the hammer signal, the inertia of the hammer prior to striking and after rebound gave a spurious signal. The spurious signal prior to impact was eliminated by triggering the data recording to begin just after impact. The movement after rebound was eliminated by digitizing the analog signal and clearing out (zeroing) the time signal after the beginning of rebound. Although the results obtained using this procedure were very repeatable, as noted, the shape and magnitude of the transfer function were sensitive to the time at which zeroing was begun. Because the immobilized transducer had a very high fundamental frequency, the time at which rebound occurred could be accurately determined during impulse hammer calibration. However, during the crossflow force transducer calibration, such knowledge was not available. The procedure followed was to clear the hammer signal after the first zero crossing: the approximate time at which rebound began.

The calibration of the crossflow force gauge was accomplished according to the schematic of Fig. A-1 utilizing the techniques developed in calibrating the force hammer. The low-pass filters and spectrum analyzer were set for a maximum frequency of 250 Hz. Also they were put in their dc mode, since the impulse hammer was found during calibration to be accurate down below 1 Hz, even though it is a piezoelectric device. The

analyzer digitized the 4.1-sec transients every 0.002 sec to give a frequency resolution 0.24 Hz. As for the hammer calibration tests, its signal was amplified by a factor of 100 for a sensitivity into the analyzer of 1.03 V/N (4.57 V/lb). Setting the bridge amplifier for the lift force at a 6-V bridge excitation, an 8.5-mV/eu sensitivity setting, a range of 1, and a tape gain of 10, the averaged transfer-function magnitude (M) and phase (P), input hammer spectrum (S), and coherence (C) (shown in Fig. 7) were obtained. Setting the drag-force bridge amplifier at the same settings as for the lift-force amplifier, except the sensitivity setting was 2.0 mV/eu, the results of Fig. 8 of the text were obtained. A calibration was also performed in air, with the same circuit settings, and the results are shown in Figs. A-3 and A-4. The HP 5451B language programs utilized to capture, analyze, and average the transient test results are given in Appendices B and C.

The desired linearity of the transducer's transfer function over the frequency range 0-50 Hz is apparent from Figs. 7, 8, A-3, and A-4. The sensitivities of the gauges in water for the bridge amplifier settings given above were determined to be: 0.855 V/N (3.79 V/lb) in the lift direction and 0.875 V/N (3.89 V/lb) in the drag direction. These are low compared to the results from the static calibration tests: 0.982 V/N (4.37 V/lb) in the lift direction and 1.062 V/N (4.72 V/lb) in the drag direction. The sensitivities of both the lift- and drag-direction transducers in air, for the bridge-amplifier settings given above, were determined to be the same as for the drag-direction transducer in water: 0.875 N/V (3.89 V/lb). The sensitivities determined in the dynamic tests were thought to be lower than those determined in the static tests because of the difficulty of striking the force-sensing ring in exactly the lift or drag direction, the inclusion of spurious hammer-head inertia effects, which would cause the force input signal to appear larger than the actual force applied, and the duplication of these effects in calibrating the force hammer. The test data were analyzed employing the static calibration, after assurance of the desired constancy of the transfer functions by dynamic calibration.

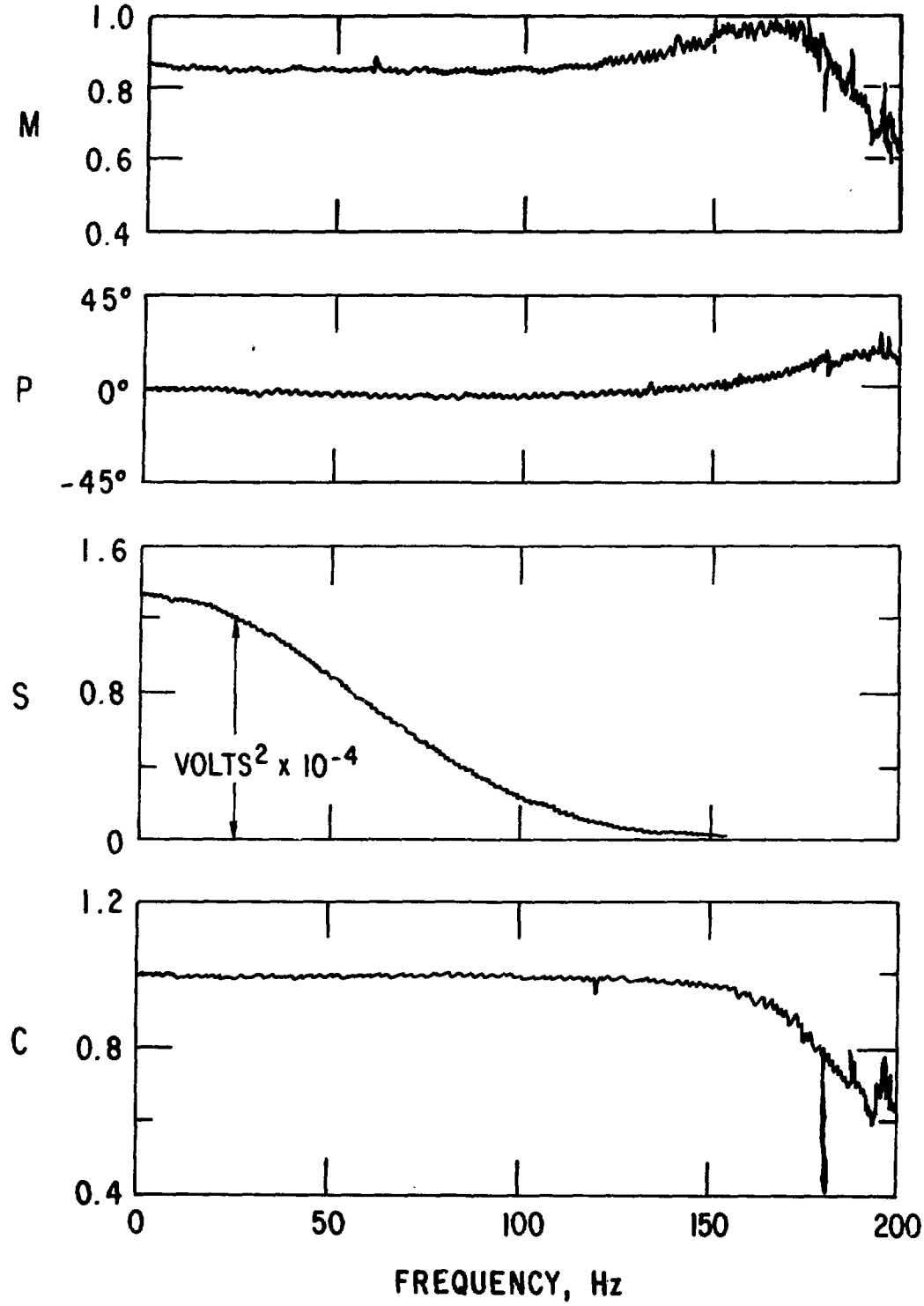

Fig. A-3. The transfer function magnitude M and phase P, input spectrum S, and coherence C for lift-direction excitation of the transducer in air

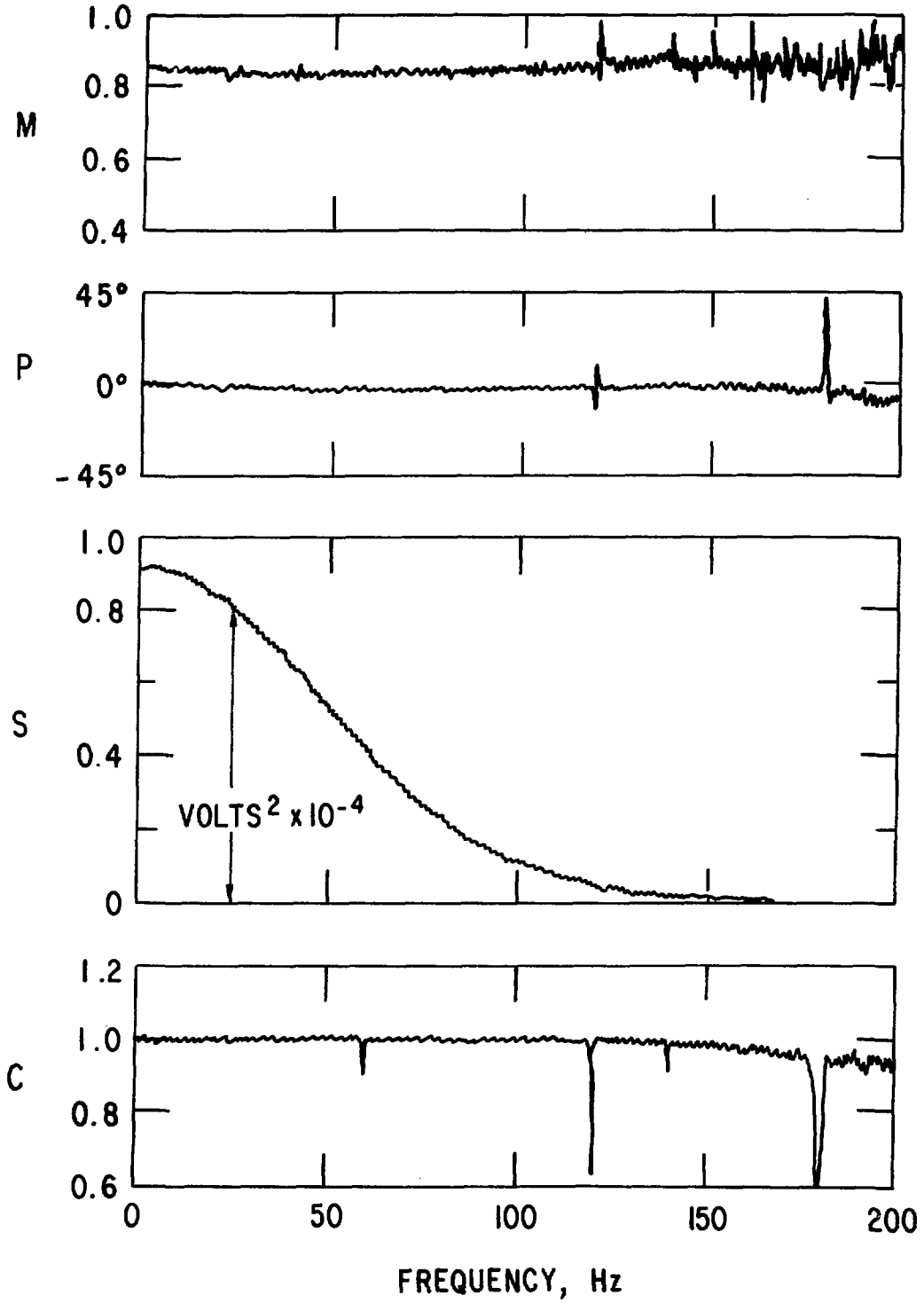

Fig. A-4. The transfer function magnitude M and phase P, input spectrum S, and coherence C for drag-direction excitation of the transducer in air

APPENDIX B - AVERAGED TRANSFER FUNCTION OF TRANSIENTS

PURPOSE

The program in Fig. B-1 determines the transfer function, coherence, input and output autospectrums, and cross spectrums for a group of time transients. The program includes steps to obtain, modify, and analyze the transients. Subsequently, the results are stored on disk for the graphic display of results with the program in Appendix C.

PARAMETERS

1. The maximum block size is 2048.
2. The program is written for 10 averages, but statements 127 and 188 can be changed to obtain results for other averages.
3. The 10 time transients selected for analysis are stored in MS 31 6 to MS 31 25, with input and outputs stored alternatively.
4. The results of the analysis are stored on disk for graphic display with program 55 as follows:

   MS 31 1 - TRANSFER FUNCTION (Channel A is input)

   MS 31 2 - COHERENCE

   MS 31 3 - INPUT SPECTRUM - (Channel A)

   MS 31 4 - OUTPUT SPECTRUM - (Channel B)

   MS 31 5 - CROSS SPECTRUM

PROGRAM (see Fig. B-1) STEPS PURPOSE

1-18	A program header is provided to start testing (see Fig. B-2 for program header MS 34 7)
20-58	After initial clearing of working blocks 0-6, the input transient is held and displayed from channels 0 to 100 in blocks 0 (A input) and 1 (B input). Also, clearing of noise from transient or other modification is allowed.
59-117	For further inspection of the transient, a single transfer function (Block 0), Coherence (Block 1), Input Spectrum (Block 2), Output Spectrum (Block 3), and Cross Spectrum (Blocks 4 (Real) and 5 (Imaginary)) are calculated. DC of the Fourier transforms are cleared in the analysis. A label is provided (MS 34 12) to instruct for inclusion or deletion of transient.

119-127 Storage commands are given for inclusion of transients and definition of loop counter (step 127) to obtain 10 averages. Different numbers of averages can be calculated by changing steps 127 and 188.

132-223 Average Transfer Function (Block 1), average Coherence (Block 2), Input Spectrum (Block 3), Output Spectrum (Block 4), Cross Spectrum [Blocks 5 (real) and 6 (imaginary)] for transients stored stored on disk beginning in MS 31 6 to MS 31 25 are calculated: clears working blocks, retrieves data, and calculates with loop counter at step 188.

224-258 Average Transfer Function, Coherence, etc., are stored on disk in MS 31 1 to MS 31 5. Header (MS 31 14) is displayed to instruct how to access coreload and program to display and document results.

```
  1 L      3
  4 MS     31      6
  8 L      2
 11 MS     34      7
 15 MS     14
 18 .
 20 L      0
 23 CL     0
 26 CL     1
 29 CL     2
 32 CL     3
 35 CL     4
 38 CL     5
 41 CL     6
 44 RA     0       1
 48 D      0       0       100
 53 D      1       0       100
 58 .
 60 X>     6
 63 X<     1
 66 X>     7
 69 X<     6
 72 F      0       1
 76 CL     0       0
 80 CL     1       0
 84 SP     0       2       2
 89 #      0       1       0
 94 CH     0       2       2
 99 *-     2       2
103 *-     3       2
107 MS     34      12
111 MS     14
114 D      0
117 .
119 MS     21      6
123 MS     21      7
127 #      2       10      0
132 CL     0
135 CL     1
138 CL     2
141 CL     3
144 CL     4
147 CL     5
150 CL     6
153 CL     7
156 MS     31      6
160 L      8
163 MS     11      1
167 MS     11      2
171 F      1       2
175 CL     1       0
179 CL     2       0
183 SP     1       2       2
188 #      8       10      0
193 CH     1       2       2
198 X<     6
201 *      0       0       1
206 A+     5
209 X>     5
212 *      3       2
216 *      4       2
220 *      5       2
224 MS     31      1
228 MS     21      1
232 MS     21      2
236 MS     21      3
240 MS     21      4
244 MS     21      5
248 MS     34      14
252 MS     14
255 CL     0
258 .
```

Fig. B-1. The transfer function program for transients in HP 5451B language

MS 34 7 - PROGRAM TO CALCULATE TRANSFER FUNCTION (AVER) IN D. PREC. SET ADC AND DISPLAY DIALS. MAXIMUM BLOCKSIZE 2048. FOR TRANSIENTS, PROGRAM WILL HALT FOR INSPECTION. HIT CONTINUE TO START.

MS 34 12 - TO INCLUDE IN AVERAGE - HIT CONTINUE. JUMP-0 FOR NEW TRANSIENT INPUT.

MS 34 14 - DATA IS NOW STORED ON DISK. TRANSFER FUNCTION, COHERENCE, INPUT, OUTPUT AND CROSS POWER SPECTRUMS ARE IN RECORDS 1-5, RESPECTIVELY. BRING DOWN PROGRAM #55 IN CORE-7 FOR GRAPHIC CAPABILITIES.

FIG. B-2. Program headers and labels

APPENDIX C - GRAPHIC ROUTINES

PURPOSE

The program (see Fig. C-1) displays and provides hard copy of the transfer function, coherence, input and output spectrum, and the cross spectrum obtained with the program of Appendix B. The results are stored on disk. Also the graphic routine displays and provides a hard copy of individual time-transient signals obtained with the Appendix B program and stores them on disk.

PARAMETERS

Parameters are normally dictated by Appendix B Program. The disk locations of the stored information are:

MS 31 1 - Transfer Function (channel A is input)

MS 31 2 - Coherence Function

MS 31 3 - Input Spectrum (channel A)

MS 31 4 - Output Spectrum (channel B)

MS 31 5 - Cross Spectrum

In MS 31 6 to 26 the Input and Output time transients are stored alternately, assuming ten tests are performed.

PROGRAM STEPS PURPOSE

1-36 A hard copy of the program header for plotting (see MS 34 20) is provided, and calculations are displayed, one at a time, for rescaling or reproductions.

37-66 The plotting routine which automatically sequences proper plot title is given. The plots utilize only 90% of area, allowing manual insertion of remarks (MS 34 28 - MS 34 36).

67-78 This is a routine which automatically provides hard copy, erases the screen, and instructs to J14 for next plot (Y5819 1).

79-90 A rescaling subroutine is given which resets ASCII text pointer for the proper title and returns the program to the plotting routine (Program Steps 37-69).

92-106 A program header is displayed (MS 34 40) and a hard copy made while the pointer is positioned to the data block (MS 31 6) containing the first time transient.

108-131 The screen is erased, header instructions (MS 34 44) for a plot are displayed, and a hard copy or a chance to rescale is provided. The time transients from the disk are loaded, and a zoom

display of the time transients (the first 100 channels) are shown.

132-162 This is a plotting routine. Only 90% of screen area is used in the plots, allowing manual insertion of remarks.

163-176 This is a hard copy routine. A hard copy is provided, the screen erased, and instructions are displayed to J16 for next time transient plot (MS 34 46).

```
  1 L       13
  4 MS      31        1
  8 MS      34       20
 12 Y     5821        6
 16 Y     5814
 19 MS     14
 22 Y     5820
 25 MS     34
 29 L      14
 32 MS     11
 35 .

 37 L      17
 40 Y     5814
 43 MS     14
 46 Y     5809
 49 Y     5804      900      900
 55 Y     5815
 58 Y     5818        1
 62 Y     5817
 65 .

 67 Y     5820
 70 Y     5814
 73 Y     5819        1
 77 .

 79 L      12
 82 MS     34       -2        1
 87 J      17
 90 .

 92 L      15
 95 MS     31        6
 99 MS     34       40
103 MS     14
106 .

108 L      16
111 Y    5814
114 MS     34       44
118 MS     14
121 MS     11
124 Y    5829        0        0      100
130 .

132 L      30
135 Y    5821        6
139 Y    5814
142 Y    5809
145 Y    5804      900      900        0
151 Y    5815
154 Y    5818        1
158 Y    5817
161 .

163 Y    5820
166 Y    5814
169 MS     34       46
173 MS     14
176 .
```

Fig. C-1. A graphics routine to display results of Appendix B program

MS 34 20 - THIS PROGRAM PLOTS: TRANSFER/COHERENCE/INPUT/OUTPUT/CROSS/PSD FORM DATA OBTAINED BY PROGRAM # 54. HIT - CONTINUE - TO PLOT. REMEMBER ! JUMP - 12 TO RESCALE. HIT - CONTINUE - FOR HARD COPY.

MS 34 28 - TRANSFER FUNCTION

MS 34 30 - COHERENCE FUNCTION

MS 34 32 - INPUT POWER SPECTRUM

MS 34 34 - OUTPUT POWER SPECTRUM

MS 34 36 - CROSSPOWER SPECTRUM

MS 34 40 - THIS PART OF PROGRAM #55 ALLOWS GRAPHIC PRESENTATION OF TRANSIENTS STORED ON DISK - FROM PROGRAM #54. HIT CONTINUE-TO START.

MS 34 44 - HIT CONTINUE - TO PLOT AND AGAIN FOR HARD COPY. JUMP - 30 TO RESCALE.

MS 34 46 - FOP NEXT PLOT - JUMP 16 -

Fig. C-2. Titles and labels